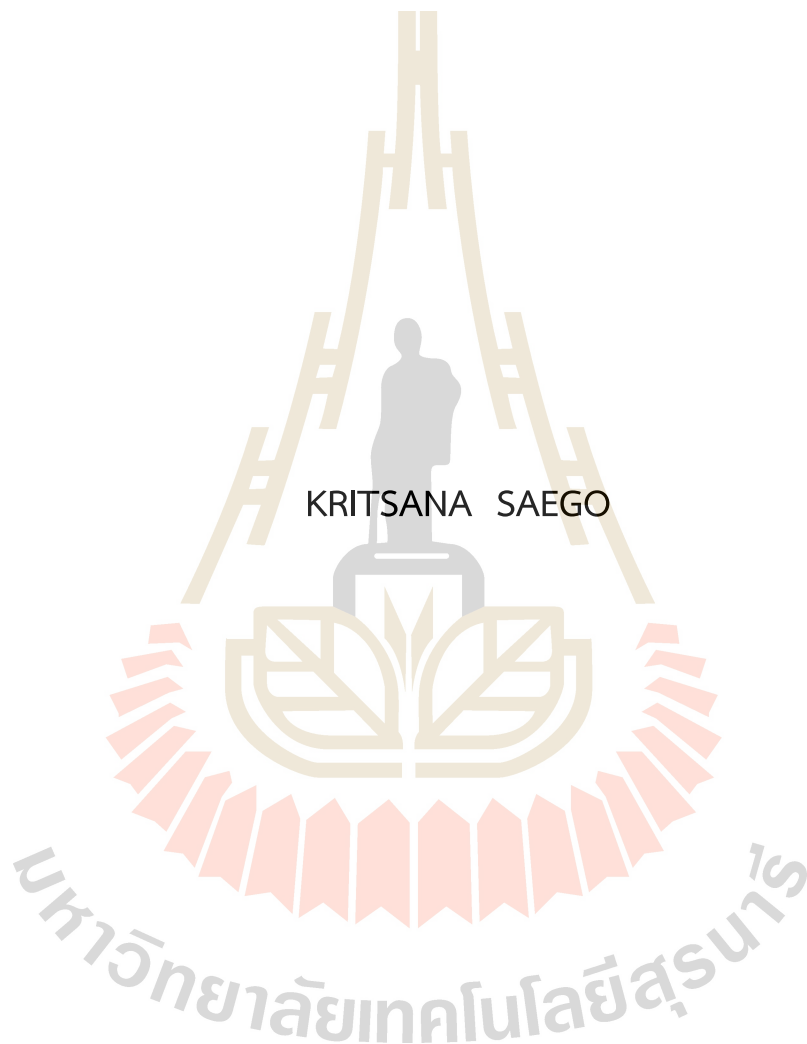


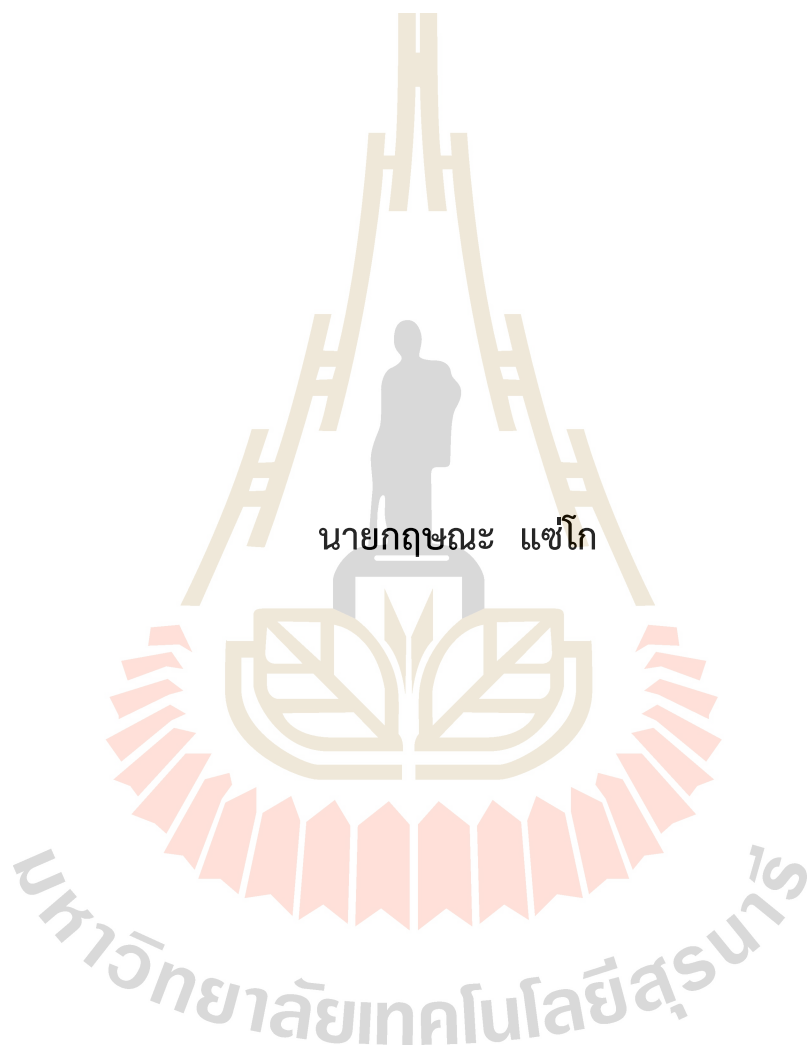
STUDY OF TWO-QUBIT INTERACTIONS IN AN ELECTRON-  
NUCLEAR SPIN QUANTUM REGISTER IN DIAMOND



KRITSANA SAEGO

A Thesis Submitted in Partial Fulfillment of the Requirements for the  
Degree of Master of Science in Physics  
Suranaree University of Technology  
Academic Year 2024

การศึกษ้อันตรกิริยาของควอนตัมบิตสองตัวในระบบควอนตัมรีจิสเตอร์  
ที่ประกอบด้วยอิเล็กตรอนและนิวเคลียสสปินในเพชร



วิทยานิพนธ์นี้เป็นส่วนหนึ่งของการศึกษาตามหลักสูตรปริญญาวิทยาศาสตรมหาบัณฑิต  
สาขาวิชาฟิสิกส์  
มหาวิทยาลัยเทคโนโลยีสุรนารี  
ปีการศึกษา 2567


STUDY OF TWO-QUBIT INTERACTIONS IN AN ELECTRON-NUCLEAR SPIN  
QUANTUM REGISTER IN DIAMOND

Suranaree University of Technology has approved this thesis submitted in  
partial fulfillment of the requirements for a Master's Degree.

Thesis Examining Committee



(Prof. Dr. Joewono Widjaja)  
Chairperson



(Dr. Sorawis Sangtawesin)  
Member (Thesis Advisor)



(Dr. Warintorn Sreethawong)  
Member



(Asst. Prof. Dr. Preeti Ovartchaiyapong)  
Member



(Assoc. Prof. Dr. Yupaporn Ruksakulpiwat)  
Vice Rector for Academic Affairs  
and Quality Assurance



(Prof. Dr. Santi Maensiri)  
Dean of Institute of Science



กฤษณะ แซ่โก : การศึกษาอันตรกิริยาของควอนตัมบิตสองตัวในระบบควอนตัมรีจิสเตอร์ที่ประกอบด้วยอิเล็กตรอนและนิวเคลียร์สปินในเพชร (STUDY OF TWO-QUBIT INTERACTIONS IN AN ELECTRON-NUCLEAR SPIN QUANTUM REGISTER IN DIAMOND) อาจารย์ที่ปรึกษา : อาจารย์ ดร.สรวิศ แสงทวีสิน, 49 หน้า.

คำสำคัญ : ตำแหน่งไนโตรเจนที่ว่างในโครงสร้างของเพชร/ กระบวนการอ่านค่าการสั่นพ้องของสนามแม่เหล็กด้วยเทคนิคเชิงแสง/ ควอนตัม/ คิวบิต/ คาร์บอนไอโซโทป 13

ตำแหน่งไนโตรเจนที่ว่าง (NV center) ในโครงสร้างของเพชรเป็นระบบสปินในสถานะของแข็งที่สามารถนำมาควบคุมให้เป็นควอนตัมบิตสำหรับการคำนวณเชิงควอนตัมได้ อย่างไรก็ตามการขยายขนาดของระบบที่มีควอนตัมบิตมากกว่าหนึ่งตัวขึ้นไปเพื่อทำเป็นควอนตัมรีจิสเตอร์นั้นยังคงเป็นปัญหาที่ท้าทายเนื่องจากตำแหน่งไนโตรเจนที่ว่างสองตำแหน่งส่วนมากมีอันตรกิริยาต่อกันไม่เพียงพอ แต่ในระบบนี้ยังมีนิวเคลียร์สปินของคาร์บอนไอโซโทป 13 ที่มีปฏิกิริยาไฮเปอร์ไฟน์กับ NV center ใกล้เคียง ซึ่งมีขนาดเพียงพอที่จะนำมาใช้เพื่อเพิ่มจำนวนของควอนตัมบิตในระบบได้ นอกจากนี้ข้อดีของการนำนิวเคลียร์สปินมาใช้ทำควอนตัมบิตคือมีระยะเวลาในการใช้งานที่ยาวนานกว่าระบบของ NV ที่มาจากอิเล็กตรอนเป็นผลมาจากการมีค่าอัตราของการหมุนในสนามแม่เหล็กที่ต่ำกว่า แต่การที่นิวเคลียร์สปินมีค่าอัตราการหมุนในสนามแม่เหล็กที่ต่ำทำให้ยากต่อการควบคุมโดยตรง ในงานวิจัยนี้ได้สาธิตการควบคุมและสังเกตพฤติกรรมของนิวเคลียร์สปินของคาร์บอนไอโซโทป 13 ที่ปฏิกิริยาไฮเปอร์ไฟน์ ขนาด 6.5 เมกะเฮิร์ตซ์ ซึ่งอาศัยเพียงการควบคุมผ่านอิเล็กตรอนโดยที่ไม่มีการใส่คลื่นวิทยุเข้าไปควบคุมนิวเคลียร์สปินโดยตรง จากผลการทดลอง เราได้ค่าอัตราการหมุนในสนามแม่เหล็กของนิวเคลียร์สปินเท่ากับ  $6.9 \pm 0.1$  กิโลเฮิร์ตซ์ต่อเกาส์ พร้อมทั้งแสดงการลดทอนของสัญญาณที่ถูกรบกวนจากสิ่งแวดล้อมโดยรอบ นอกจากนี้เรายังรายงานข้อมูลเฟสของนิวเคลียร์สปินที่ถูกสะสมในชั้นพลังงานของอิเล็กตรอนสปิน  $m_s = -1$  และประยุกต์นำผลตรงนี้มาใช้ในการควบคุมเฟสของนิวเคลียร์สปิน ในส่วนสุดท้ายเรายังแสดงให้เห็นถึงความไม่สมบูรณ์ของการถ่ายโอนประชากรของสปินที่จะเป็นประโยชน์ต่อการพัฒนาระบบให้ดีขึ้นในอนาคตอีกด้วย



KRITSANA SAEGO : STUDY OF TWO-QUBIT INTERACTIONS IN AN ELECTRON-NUCLEAR SPIN QUANTUM REGISTER IN DIAMOND. THESIS ADVISOR : SORAWIS SANGTAWESIN, Ph.D. 49 PP.

Keyword: NV center in diamond/optically detected magnetic resonance (ODMR)/quantum/ qubit/  $^{13}\text{C}$  nuclear spins

The nitrogen vacancy (NV) center in diamond is one of the solid-state spin systems that can be manipulated as a qubit for quantum computing. However, scaling up the system to perform as a quantum register is challenging due to the weak dipole interaction between two NV centers. On the other hand,  $^{13}\text{C}$  nuclear spins that reside within the diamond lattice can be used as additional qubits for scaling up the system, as they have hyperfine interactions with the NV center electronic spin. In general, nuclear spins exhibit a longer coherence time compared to the electron spin due to the lower gyromagnetic ratio. Nevertheless, this weak interaction also makes it difficult to directly control the nuclear spin. In this work, we demonstrated a scheme to control and observe the dynamics of nuclear spin with a hyperfine splitting of 6.5 MHz using an indirect pulse sequence that operated only the electron spin in absence of any RF signal. Our results reveal a nuclear spin free precession with a gyromagnetic ratio of  $6.9 \pm 0.1$  kHz/Gauss and signal decay from the environment noise. Furthermore, one can observe the nuclear spin phase accumulation in electronic spin  $m_s = -1$  manifold and apply it to control their phase. Finally show the reduced contrast results from incomplete population transfer during the operation that can be improved in the future.

School of Physics  
Academic Year 2024

Student's signature นางสาว: วนิดา  
Advisor's signature ศาสตราจารย์: สรวิช

## ACKNOWLEDGEMENTS

I would like to express my deepest gratitude to my advisor, Dr. Sorawis Sangtawesin, for his invaluable guidance, support, and encouragement throughout the course of my research. His expertise and insights have been instrumental in shaping the direction and quality of this work. I am deeply appreciative of his patience and dedication in mentoring me through each stage of this thesis.

I would also like to extend my sincere thanks to my thesis defense committee members: Prof. Joewono Widjaja, Dr. Warintorn Sreethawong, and Assist. Prof. Preeti Ovarthaiyapong. Your thoughtful feedback, constructive criticism, and valuable suggestions have greatly contributed to the improvement and completion of this work.

My heartfelt thanks go to the members of the research groups QLAB, OCT, and Meevasana. Your collaboration, support, and stimulating discussions have greatly enriched my research experience.

Importantly, I would like to acknowledge the Development Program in Science and Technology (DPST) for providing financial support while pursuing my bachelor's degree. This research has also received funding support from the NSRF via the Program Management Unit for Human Resources & Institutional Development, Research, and Innovation [Grant numbers B05F650024, B37G660011].

Additionally, special thanks go to all of my friends for their unwavering support and encouragement, which have been a constant source of strength and motivation. Finally, I thank my family for standing by me during the hard times throughout my studies.

Kritsana Saego

## CONTENTS

	Page
ABSTRACT IN THAI.....	I
ABSTRACT IN ENGLISH.....	II
ACKNOWLEDGEMENTS.....	III
CONTENTS.....	IV
LIST OF TABLES.....	VII
LIST OF FIGURES.....	VIII
<b>CHAPTER</b>	
<b>I INTRODUCTION.....</b>	<b>1</b>
1.1 Background and motivation .....	1
1.2 Research objective.....	3
1.3 Scope of thesis.....	3
1.4 Outline of thesis.....	3
<b>II LITERATURE REVIEWS .....</b>	<b>5</b>
2.1 Qubit.....	5
2.2 Quantum logic gates.....	6
2.2.1 Single-qubit gate.....	6
2.2.1.1 The X gate, Y gate and Z gate.....	6
2.2.1.2 The Hadamard gate.....	7
2.2.2 Two-qubit Controlled NOT (CNOT) gate.....	7
2.2.3 Universal set of Quantum gates.....	9

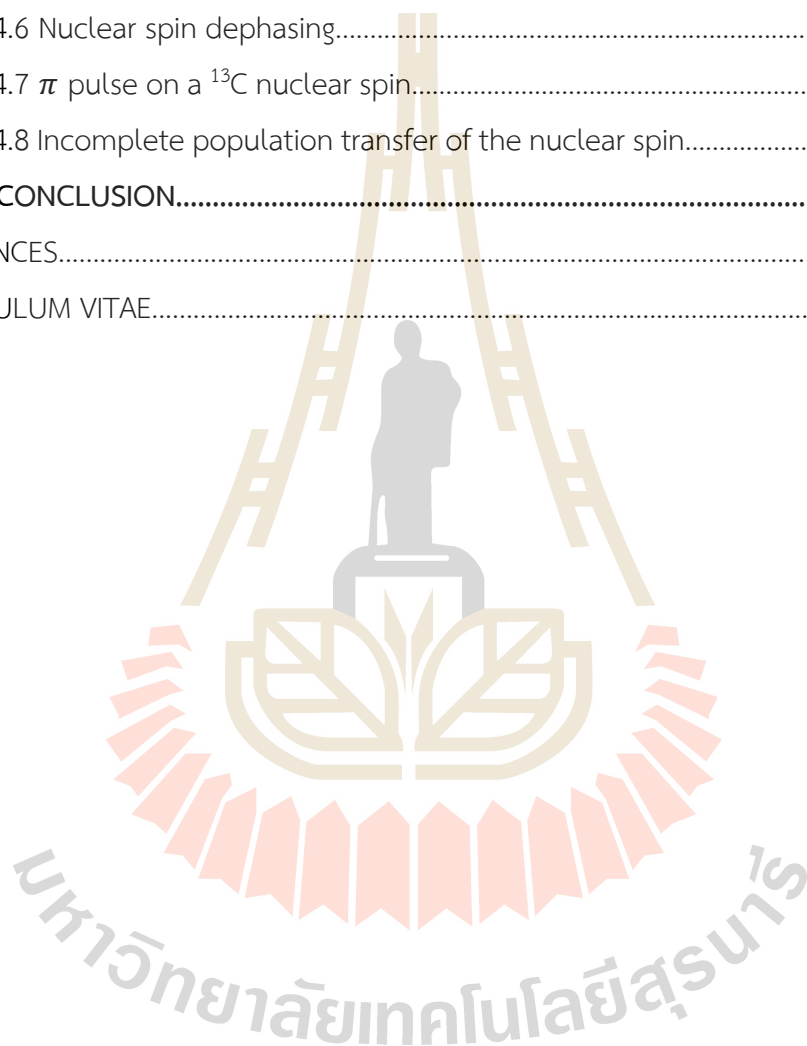


## CONTENTS (Continued)

		Page
	2.3 Decoherence.....	9
	2.3.1 The relaxation time ( $T_1$ ) .....	9
	2.3.2 The dephasing time ( $T_2$ ) .....	9
	2.4 Quantum control process.....	10
	2.4.1 Rabi Oscillation.....	10
	2.4.2 Ramsey experiment .....	13
	2.4.3 Spin echo.....	14
	2.5 Nitrogen-vacancy center .....	16
	2.5.1 Energy Diagram of the NV center.....	17
	2.5.2 NV center Hamiltonian.....	19
	2.5.3 The hyperfine coupling between $^{13}\text{C}$ and the NV center.....	20
<b>III</b>	<b>RESEARCH METHODOLOGY.....</b>	<b>23</b>
	3.1 NV center Sample.....	23
	3.2 Acousto-Optic Modulator (AOM) setup.....	23
	3.3 Single-Photon Confocal microscope.....	25
	3.4 Microwave-control system.....	27
	3.5 Pulse experiment for NV center experiment.....	28
<b>IV</b>	<b>RESULTS AND DISCUSSION.....</b>	<b>30</b>
	4.1 The single NV picture from the confocal microscope.....	30
	4.2 Optically detected magnetic resonance (OMDR).....	31
	4.2.1 Zero field signal.....	31
	4.2.2 Zeeman-splitting signal.....	32
	4.2.3 Hyperfine splitting signal.....	33
	4.3 Rabi experiment.....	34

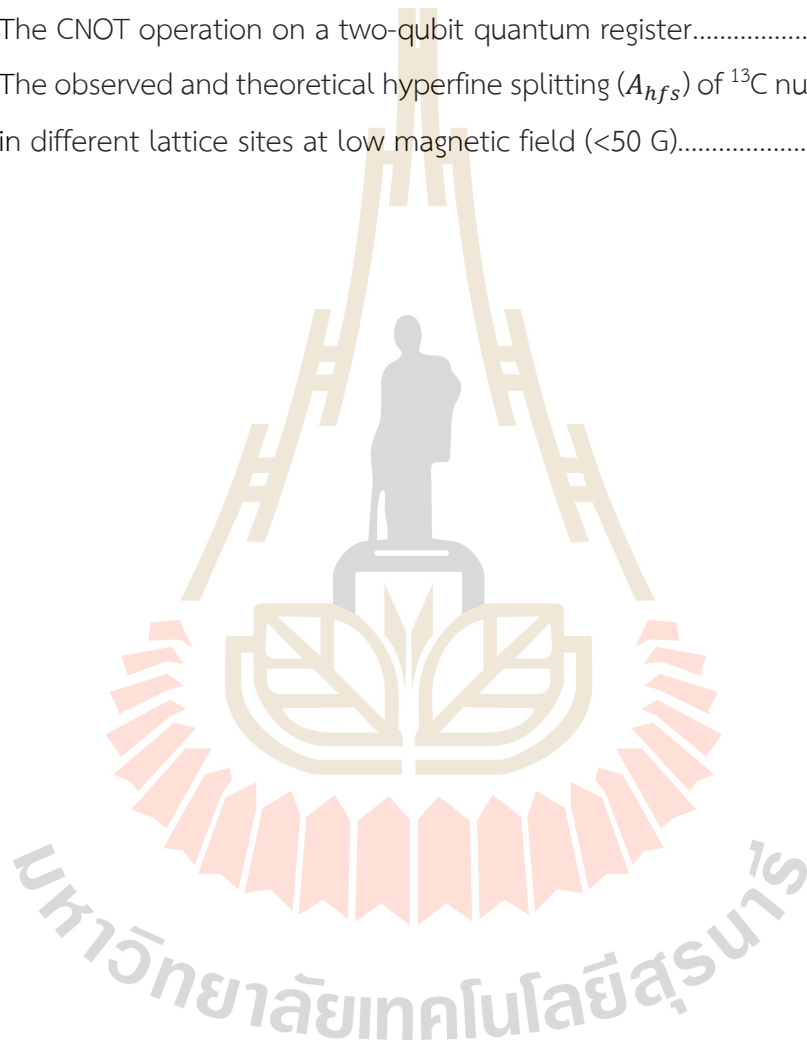
## CONTENTS (Continued)

	Page
4.4 Nuclear free precession data.....	36
4.5 Nuclear Ramsey experiment.....	38
4.6 Nuclear spin dephasing.....	39
4.7 $\pi$ pulse on a $^{13}\text{C}$ nuclear spin.....	40
4.8 Incomplete population transfer of the nuclear spin.....	42
<b>V CONCLUSION.....</b>	<b>44</b>
REFERENCES.....	45
CURRICULUM VITAE.....	50



## LIST OF TABLES

Table		Page
2.1	The CNOT operation on a two-qubit quantum register.....	2
2.2	The observed and theoretical hyperfine splitting ( $A_{hfs}$ ) of $^{13}\text{C}$ nuclear spin in different lattice sites at low magnetic field (<50 G).....	3





## LIST OF FIGURES

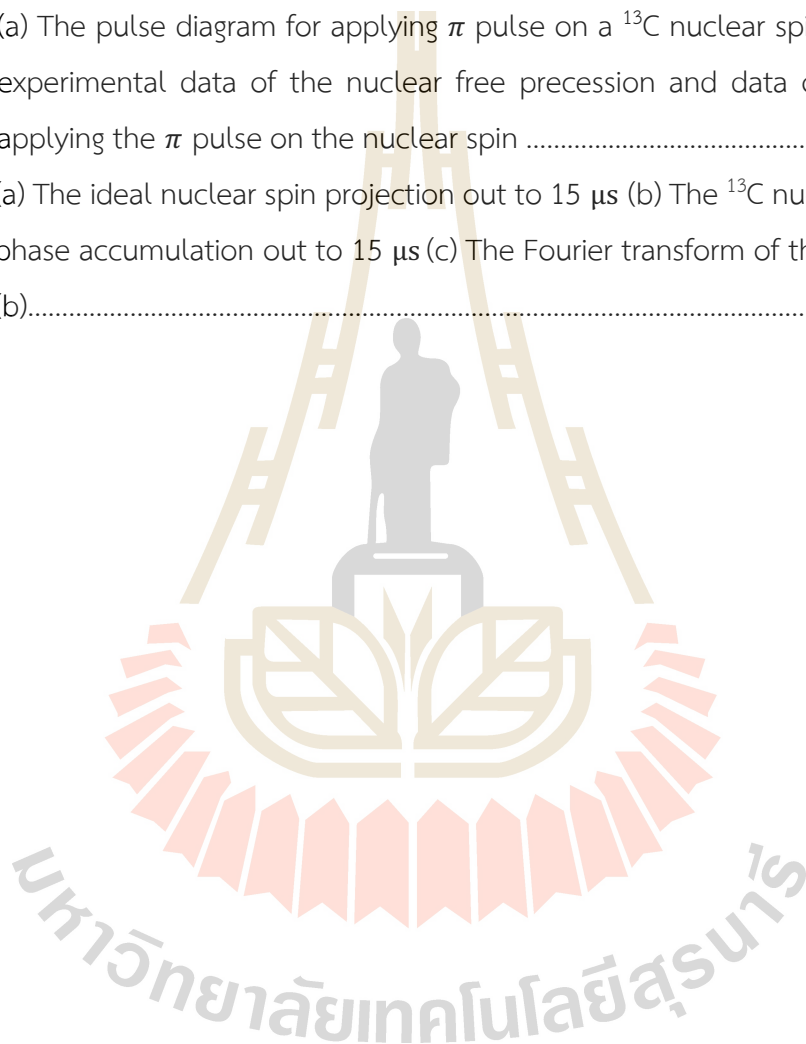
Figure	Page
2.1 The Bloch sphere representation for visualizing the qubit state.....	6
2.2 The evolution of the qubit state after operated by the X-gate, the Y-gate, the Z-gate, and the Hadamard gate.....	7
2.3 The quantum circuit for generating the two-qubits entanglement in form $\frac{1}{\sqrt{2}}( 00\rangle +  11\rangle)$ .....	8
2.4 The relaxation time ( $T_1$ ) and the dephasing time ( $T_2$ ).....	10
2.5 (a) The Bloch sphere visualization for the Rabi oscillation behavior (b) The graph shows the ideal behavior of the Rabi oscillation signal.....	12
2.6 (a) Pulse sequence for the Ramsey experiment (b) The process and the state evolution of the qubit in the Ramsey experiment.....	13
2.7 (a) Pulse diagram for spin echo experiment (b) The process and the state evolution of the qubit in the spin echo process.....	15
2.8 NV <sup>-</sup> system that is caused by the substitution of one carbon atom with a nitrogen atom.....	16
2.9 The energy level diagram for the NV center (a) Electron start in spin $m_s = 0$ (b) For electron starts in spin $m_s = \pm 1$ .....	17
2.10 The fluorescence emission from the NV center.....	18
2.11 The photoluminescence is dependent on the number of spin states.....	19
2.12 The Zeeman-splitting effect on the electron in the NV center.....	20
2.13 (a) The energy diagram for the coupling between the electron spin and nuclear spin from $^{13}\text{C}$ (b) This is the ODMR result that show the transition of the $^{13}\text{C}$ .....	21
2.14 Visual representation showcasing the geometry of the NV defect from two perspectives (Smeltzer et al., 2011).....	22

## LIST OF FIGURES (Continued)

Figure	Page
3.1 (a) Diagram of the AOM setup. (b) The outputs of the green laser when turn off (left) and turn on (right) the AOM.....	24
3.2 Diagram of the confocal microscope setup.....	25
3.3 Picture of the confocal microscope setup.....	26
3.4 Diagram for the microwave control system.....	27
3.5 The microwave signal before and after passing the NV sample.....	28
3.6 (a) The whole picture for the NV center experiment. (b) The diagram for the NV center pulsed experiment.....	29
4.1 The picture of the diamond surface that was taken by the confocal microscope.....	31
4.2 (a) A pulse sequence for ODMR experiment (b) Zero-field splitting signal	32
4.3 (a) Installation of magnet into the setup (b) Zeeman-splitting signal at magnetic field $B_z = 23$ G.....	33
4.4 (a) pulsed-ODMR diagram. (b) The pulsed-ODMR result at magnetic field $B_z = 46$ G.....	34
4.5 (a) The energy diagram for the coupled NV center electron spin and nuclear spin of the $^{13}\text{C}$ (b) Rabi experiment pulse sequence (c) The electron Rabi oscillation data obtained by driving the resonance frequencies of the weak (blue) and strong (red) microwaves.....	35
4.6 (a) Diagram representation spin state evolution during the nuclear free precession operation (b) Nuclear free precession graph in a magnetic field $B_z = 46$ G (c) The Larmor precession frequency of the single nuclear spin.....	37
4.7 (a) The pulse experiment diagram for observing the phase accumulation of the nuclear spin. (b) Nuclear spin projection shows oscillation with frequency $2\pi \cdot 6.5$ MHz.....	38

## LIST OF FIGURES (Continued)

Figure		Page
4.8	(a) The nuclear free precession data out to 250 $\mu\text{s}$ (b) Nuclear spin projection shows oscillation with frequency $2\pi \cdot (6.5)$ MHz .....	39
4.9	(a) The pulse diagram for applying $\pi$ pulse on a $^{13}\text{C}$ nuclear spin (b) The experimental data of the nuclear free precession and data obtain by applying the $\pi$ pulse on the nuclear spin .....	41
4.10	(a) The ideal nuclear spin projection out to 15 $\mu\text{s}$ (b) The $^{13}\text{C}$ nuclear spin phase accumulation out to 15 $\mu\text{s}$ (c) The Fourier transform of the data in (b).....	43





# CHAPTER I

## INTRODUCTION

### 1.1 Background and motivation

The nitrogen-vacancy (NV) center is one of the solid-state spin systems that can be implemented in quantum technology, produced by replacing two of the carbon atoms in the diamond structure with a nitrogen atom and an adjacent vacancy. The negatively-charged NV center contains a spin triplet system (Doherty et al., 2013; Jeske et al., 2017), which can be controlled using microwave pulse techniques and read out via an optical signal in ambient conditions (Childress et al., 2006). Moreover, compared to other quantum systems, the NV center system is more affordable to develop, with a demonstration laboratory experiment costing about of \$20,000 (Sewani et al., 2020).

In quantum computing, the NV center is of interest because it has a long coherence time in order of milliseconds (Castelletto et al., 2012). However, to scale the qubit up to many numbers of the NV centers, there is a limitation that the distance has to be shorter than 25 nm to make the entanglement between two NV centers (Dolde et al., 2013), which prohibits optical addressing of each NV center with standard techniques. However, due to the coupling between the electron from NV center and the surrounding nuclear spins such as  $^{13}\text{C}$ ,  $^{14}\text{N}$ , and  $^{15}\text{N}$ , we can use these nuclear spins to increase the number of qubits in the quantum register, while using only a single NV center. In general, the nuclear spin qubit has a longer coherence time than the electron spin because the nuclear spin has a lower gyromagnetic ratio than the electron spin (Dutt, Childress et al., 2007; Maurer et al., 2012), making it a robust quantum memory in the quantum register.

Various techniques in NV studies have been developed from other research, however; there are limitations in studying  $^{13}\text{C}$  nuclear spin. Jiang et al. (Jiang et al., 2009) reported the protocol to control and repeatedly read out the signal from up to three qubits, using the  $^{13}\text{C}$  nuclear spins. The quantum register derived from these surrounding nuclear spins proves effective for quantum error correction (QEC), a crucial step in quantum computer development. However, this protocol is quite challenging, as it requires the search from over 3,300 NV centers to find the appropriate coupling parameters with two  $^{13}\text{C}$  nuclei suitable for qubits in the QEC protocol (Waldherr et al., 2014). Sangtawesin et al. (Sangtawesin et al., 2014) performed a fast phase gate at room temperature on the  $^{14}\text{N}$  nuclear spin, which is challenging to control due to its small nuclear magnetic moment. Furthermore, it can be difficult to control the nuclear spin of especially when working with additional weak coupling interactions of  $^{13}\text{C}$ . Taminiau et al. (Taminiau et al., 2012) showed access and control up to six qubits from weakly coupled nuclear spins using the dynamical microwave pulse technique, and later the group had extended the protocol towards a ten-qubit quantum register (Bradley et al., 2019). Even though several techniques were proposed to access the control of nuclear spin in NV center system, they are inconvenient to deal with and require the use of RF signals for direct nuclear spin manipulation.

Several studies have attempted to control hybrid systems by leveraging interactions and using microwave control of electrons and nuclear spins together (Dutt et al., 2007; Kegami et al., 2011; Zhang et al., 2019). In this study, we demonstrated indirect control of nuclear spin without applying RF signals, following the protocol outlined in Dutt et al. shows the observation of free precession of the nuclear spin and hyperfine effects. Additionally, we investigated the effects of poor polarization at this point to find techniques in the future to mitigate these effects and improve our system.

## 1.2 Research objectives

- 1.2.1 To study and observe the dynamics of electron and  $^{13}\text{C}$  nuclear spin in the nitrogen-vacancy center.
- 1.2.2 To coherently control an electron-nuclear spin system as a quantum register.
- 1.2.3 To perform the  $^{13}\text{C}$  nuclear spin phase gate by using the hyperfine interaction.

## 1.3 Scope of thesis

- 1.3.1 We focus on only the coupling between electron spin from the NV center and a nuclear spin from  $^{13}\text{C}$ .
- 1.3.2 We perform all the experiments at room temperature.

## 1.4 Outline of thesis

This thesis is divided into five main chapters. Chapter I is the introduction consisting of the background and motivation, research objectives, and scope of this thesis. In chapter II, we describe the basic theories and properties of the qubit and the process to control it. Moreover, we introduce the NV center, which is the system that was used in this thesis, including the energy diagram and the Hamiltonian for describe the dynamics of the system. In chapter III, we show the setup and procedures used in this work. The diagram of a single-photon confocal microscope and a microwave setup for observing and controlling the NV center are shown in this part. In addition, the description for the microwave pulsed experiment also shown in this chapter. Chapter IV presents the experimental results of the thesis consisting of the NV center picture taken from the confocal microscope; the optically detected magnetic resonance (ODMR), showing the zero field and Zeeman splitting of the NV center. Furthermore, we performed the pulsed-ODMR to characterize the electronic spin of the NV center coupled with nuclear spin. After that, we show the results from controlling the electron spin and the  $^{13}\text{C}$  nuclear spin such as the Rabi oscillation, the free precession and Ramsey experiment of the  $^{13}\text{C}$  nuclear spin. Additionally, we investigated the effects



of poor polarization to find techniques in the future to mitigate these effects and improve our system. Finally, the conclusion of this thesis is given in Chapter V.



## CHAPTER II

### LITERATURE REVIEWS

In this section, we describe the details of a qubit in a quantum computer, including the Bloch sphere representation and the gate set required for qubit operation. In addition, we explain the concept and fundamental mathematics of quantum processes such as the Rabi process, the Ramsey process, and the spin echo process. Furthermore, the final section will provide background information for our candidate quantum system, the nitrogen-vacancy center.

#### 2.1 Qubit

A qubit, or quantum bit, is a fundamental unit in quantum computing. In a classical computer, the information is represented by a "classical bit," which has only two logic values, 0 and 1. On the other hand, the qubit can store information in terms of superposition between bits 0 and 1 at the same time. Moreover, it has phase information on each state, which the classical bit cannot provide. We can visualize a qubit state using a Bloch sphere (Nielsen et al., 2004). As shown in figure 2.1, a pure qubit state can exist anywhere on the Bloch sphere surface. This property provides a qubit with a more powerful computation resource compared with the classical bit. In general, the qubit can be written in formal notation, as shown below.

$$|\psi\rangle = \cos\frac{\theta}{2}|0\rangle + e^{i\varphi}\sin\frac{\theta}{2}|1\rangle \quad (1)$$

Where state,  $|0\rangle = \begin{pmatrix} 1 \\ 0 \end{pmatrix}$  and  $|1\rangle = \begin{pmatrix} 0 \\ 1 \end{pmatrix}$  are the matrix that satisfies the orthonormal properties.  $\theta$  and  $\varphi$  are defined according to the spherical coordinates on the Bloch sphere.

On the Bloch sphere, state  $|0\rangle$  and  $|1\rangle$  are located at the north and south poles, respectively. In addition, there are two orthogonal pair of pure states on the equator of the Bloch sphere, namely state  $|\pm\rangle = \frac{1}{\sqrt{2}}(|0\rangle \pm |1\rangle)$  and state  $|\pm i\rangle = \frac{1}{\sqrt{2}}(|0\rangle \pm i|1\rangle)$  that are on opposite sides of the Bloch sphere.

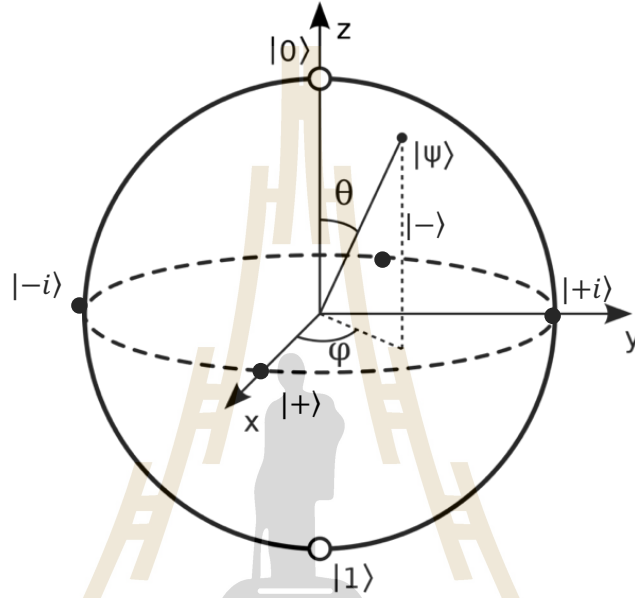


**Figure 2.1** The Bloch sphere representation for visualizing the qubit state, the state  $|0\rangle$  and  $|1\rangle$  are on the top and the bottom of the z axis. Two set of orthogonal bases  $|\pm\rangle$  and  $|\pm i\rangle$  are located on the xy-plane of the Bloch sphere.

## 2.2 Quantum logic gates

### 2.2.1 Single-qubit gate

The purpose of the qubit control is to project the qubit state to any location on the Bloch sphere. Quantum gates are unitary operations required to transfer the state of a qubit. Here, we describe a list of some necessary gates for a single qubit.

#### 2.2.1.1 The X gate, Y gate and Z gate

The X-gate or NOT gate is represented by the Pauli-X  $\sigma_x = \begin{pmatrix} 0 & 1 \\ 1 & 0 \end{pmatrix}$  matrix. The operation of this gate is to switch the coefficient between state  $|0\rangle$  and  $|1\rangle$ , so we can

call the X-gate as bit flip gate. The Y-gate is represented by the Pauli-Y  $\sigma_y = \begin{pmatrix} 0 & -i \\ i & 0 \end{pmatrix}$  matrix, which is used to rotate a quantum state  $180^\circ$  around the Y-axis of the Bloch sphere. The Z-gate is represented by the Pauli-Z  $\sigma_z = \begin{pmatrix} 1 & 0 \\ 0 & -1 \end{pmatrix}$  matrix. This gate causes the qubit to rotate  $180^\circ$  around the Z-axis, in this operation, it switches the phase of the qubit, so this gate is often called the phase-flip gate.

### 2.2.1.2 The Hadamard gate

The Hadamard is used to generate the superposition between state  $|0\rangle$  and  $|1\rangle$ . The operation of this gate is rotating the qubit  $90^\circ$  around the Y-axis, followed by a  $180^\circ$  rotation around the X-axis.

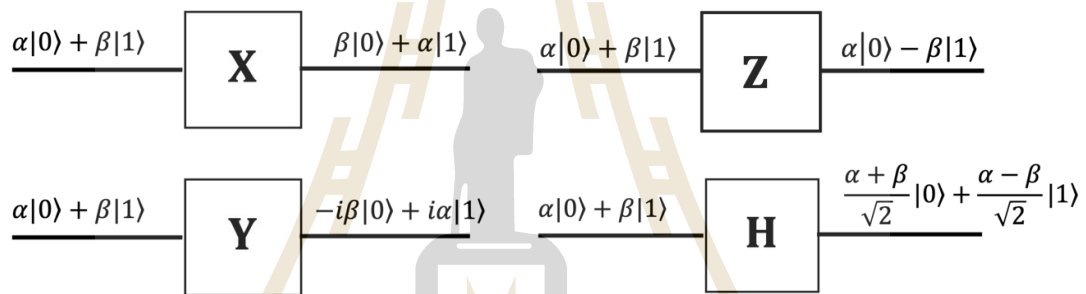


**Figure 2.2** This figure shows the evolution of the qubit state after operated by each gate. The X-gate is used to map the state  $|0\rangle$  to  $|1\rangle$  and state  $|1\rangle$  to  $|0\rangle$ . Similarly, the Y-gate map state  $|0\rangle$  to  $i|1\rangle$  and state  $|1\rangle$  to  $-i|0\rangle$ . The Z-gate does nothing to state  $|0\rangle$  but creates the phase  $\pi$  to state  $|1\rangle$  as  $-|1\rangle$ . And the Hadamard gate create the superposition state from the Z basis.

### 2.2.2 Two-qubit Controlled NOT (CNOT) gate

In general, for many qubits, some gates can be constructed by using the tensor product of multiple single-qubit gates. However, some of gate cannot be constructed such as controlled-NOT (CNOT) gate.



The CNOT gate operates on a two-qubit quantum register. When the first qubit (control qubit) is in state  $|1\rangle$ , it is used to switch the state of the second qubit (or target qubit). The CNOT gate's operations are detailed in the table 2.1.

**Table 2.1** The CNOT gate operation on a two-qubit quantum register.

Before		After	
Control qubit	Target qubit	Control qubit	Target qubit
0	0	0	0
0	1	0	1
1	0	1	1
1	1	1	0

Example). Generating two-qubits entanglement

Figure 2.3 shows the quantum circuit that was used to generate the two-qubit entanglement. First, the two qubits are prepared in state  $|0\rangle$ , so the total state is in the tensor product form  $|0\rangle \otimes |0\rangle$ . By only operating the first qubit with the Hadamard gate, making it is in superposition between state  $|0\rangle$  and state  $|1\rangle$ . The total state will be  $\frac{1}{\sqrt{2}}(|0\rangle + |1\rangle) \otimes |0\rangle$ . After that, apply a CNOT gate to change the state of the second qubit from state  $|0\rangle$  to state  $|1\rangle$ , the final state will be in form  $\frac{1}{\sqrt{2}}(|00\rangle + |11\rangle)$ .

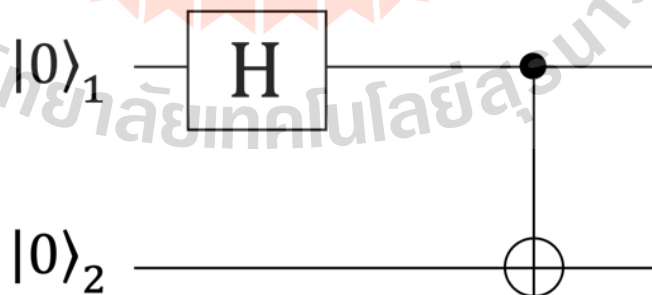


**Figure 2.3** The quantum circuit for generating the two-qubits entanglement in form  $\frac{1}{\sqrt{2}}(|00\rangle + |11\rangle)$ .

### 2.2.3 Universal set of Quantum gates

A universal set of quantum gates is a set of gates that enables the implementation of any quantum operation and is an essential component of quantum computing to enable a wide variety of quantum algorithms and computations (Grover, 1997; Zhang, S., and Li, L., 2022).

The controlled-NOT (CNOT) gate and the single-qubit gates are examples of a complete set of universal quantum gates. Any desired unitary transformation can be approximated by combining single-qubit operations with CNOT gates. For example, we can use the Hadamard gate to produce a superposition state, followed by a CNOT gate to generate an entanglement between two qubits.

## 2.3 Decoherence

The decoherence is the mechanism or process that makes the quantum state lose the phase information from the state and revert to the classical state, which is a result of multiple factors, including coupling from the spin bath, temperature noise, magnetic flux noise and sensitive parameters from outside the system. This is the important factor we need to characterize in order to create a qubit. The set of decoherences in the qubit is shown below.

### 2.3.1 The relaxation time ( $T_1$ )

The relaxation time or decoherence resulting from a perturbation orthogonal to the quantization axis or rotation about the x and y axes on the Bloch sphere. The simplest explanation for this parameter is the time required for the electron in excited state decay to the ground state (i.e., Transmon/Atom) as shown in figure 2.4(a).

### 2.3.2 The dephasing time ( $T_2$ )

The dephasing time is a result from a perturbation along the quantization axis or the rotation around the z axis on the Bloch sphere, for example, magnetic flux noise that causes phase randomization in the superconducting qubits (Ithier, Collin et al.

2005). In figure 2.4(b), the states on the equator of the Bloch sphere of the qubit can store the information of the phase difference between state  $|0\rangle$  and state  $|1\rangle$  of the qubit.

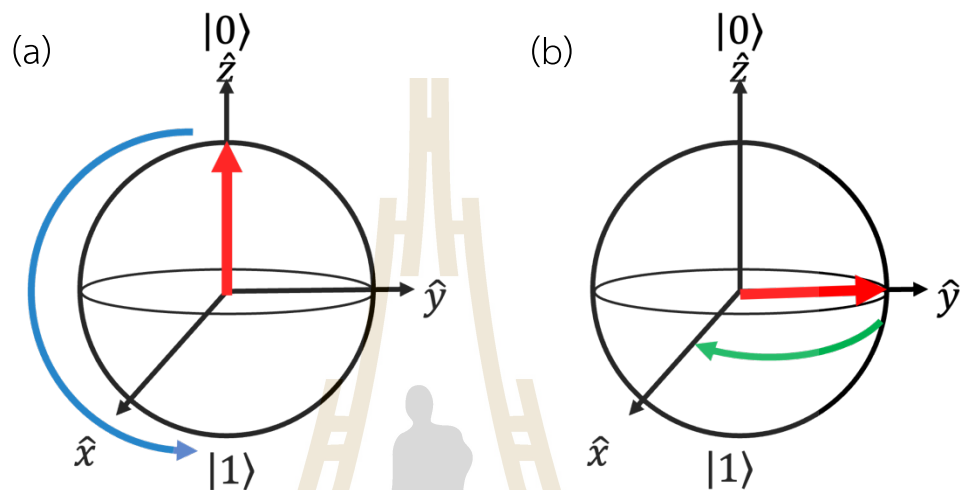


**Figure 2.4** (a) This figure illustrates the behavior of relaxation time as the qubit travels from the north pole to the south pole of the Bloch sphere. (b) To describe about the dephasing process, the qubit stores phase information, and the dephasing behavior gives us an estimate of the time required for the qubit to lose the phase information.

## 2.4 Quantum control process

To control qubits in the quantum computer, we need to perform quantum processes to characterize and manipulate our system.

### 2.4.1 Rabi Oscillation

The Rabi oscillation is the oscillation of the basis state in a quantum two-level system when an external AC field is applied as shown in figure 2.5(a). In quantum computing, we use the Rabi process to flip the qubit from state  $|0\rangle$  to  $|1\rangle$ . This part is necessary for controlling the qubits.

Suppose we have a two-level system with transition energy  $\omega_0$  that is under an oscillating magnetic field of angular frequency  $\omega$ . The dynamics of the system can be described by the Hamiltonian (Nakahara Mikio, 2008) (Here we use  $\hbar = 1$  for simplicity)

$$H = -\frac{\omega_0}{2}\sigma_z + \frac{\omega_1}{2}(\cos(\omega t)\sigma_x - \sin(\omega t)\sigma_y) \quad (2)$$

$$= -\frac{\omega_0}{2}\begin{pmatrix} 1 & 0 \\ 0 & -1 \end{pmatrix} + \frac{\omega_1}{2}\begin{pmatrix} 0 & e^{i\omega t} \\ e^{-i\omega t} & 0 \end{pmatrix}, \quad (3)$$

where  $\omega_1 > 0$  is a parameter proportional to the amplitude of the oscillating field. By setting the initial state in the ground state of the unperturbed Hamiltonian as

$$|\psi(0)\rangle = |0\rangle. \quad (4)$$

By tuning  $\omega = \omega_0$  (Resonance frequency) and performing a unitary transformation, the time evolution of the state can be expressed as

$$|\psi(t)\rangle = \begin{pmatrix} e^{i\omega_0 t/2} \cdot \cos\left(\frac{\omega_1 t}{2}\right) \\ -ie^{-i\omega_0 t/2} \cdot \sin\left(\frac{\omega_1 t}{2}\right) \end{pmatrix} \quad (5)$$

$$= e^{i\omega_0 t/2} \left( \cos\left(\frac{\omega_1 t}{2}\right) |0\rangle - ie^{-i\omega_0 t} \sin\left(\frac{\omega_1 t}{2}\right) |1\rangle \right). \quad (6)$$

From this result, the quantum state will repeatedly oscillate from  $|0\rangle$  to  $|1\rangle$ . The term  $e^{i\omega_0 t/2}$  is called the “global phase” term which is the phase in common between two states and does not affect the measurement of a single qubit. The term  $ie^{-i\omega_0 t}$  is the relative phase between state  $|0\rangle$  and  $|1\rangle$ , which shows the evolution of the state with respect to time.

This oscillatory behavior is called the Rabi oscillation, and the frequency  $\omega_1$  is called the Rabi frequency. We can find the probability of finding the final state in terms of the sine and cosine function as shown below.

$$P_0 = 1 - \sin^2\left(\frac{\omega_1 t}{2}\right) \quad (7)$$

$$P_1 = \sin^2\left(\frac{\omega_1 t}{2}\right) \quad (8)$$

Where  $P_0$  and  $P_1$  are probability to get the qubit in state  $|0\rangle$  and  $|1\rangle$  respectively. From equation (7) and (8), the population of the qubit in state  $|0\rangle$  and state  $|1\rangle$  are shown in figure 2.5(b).

From the graph in figure 2.5(b), we can prepare the qubit in any state by applying specific time of signal control. For example, we can prepare the qubit in state  $|1\rangle$  by applying the control signal with time  $t = \frac{\pi}{\omega_1}$ .

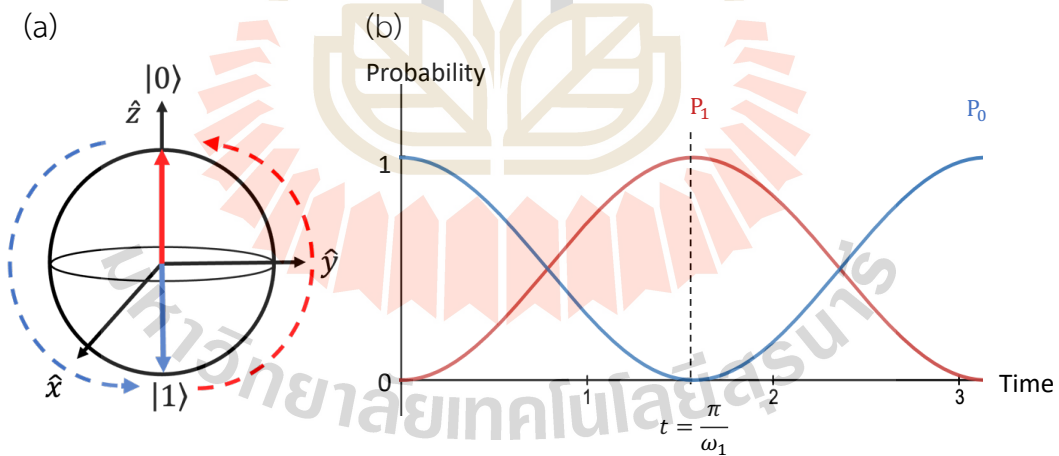


**Figure 2.5** (a). The Bloch sphere visualization for the Rabi oscillation behavior. (b). The graph shows the ideal behavior of the Rabi oscillation signal. The probability to get state  $|0\rangle$  and  $|1\rangle$  from the qubit will oscillate with sine and cosine function with respect to time.

### 2.4.2 Ramsey experiment

As mentioned in section 2.1, the qubit can store information in phase term represented by the azimuthal location  $\varphi$  on the Bloch sphere. Ramsey measurement is the process that is used to observe the phase accumulation and the decoherence of the qubits.

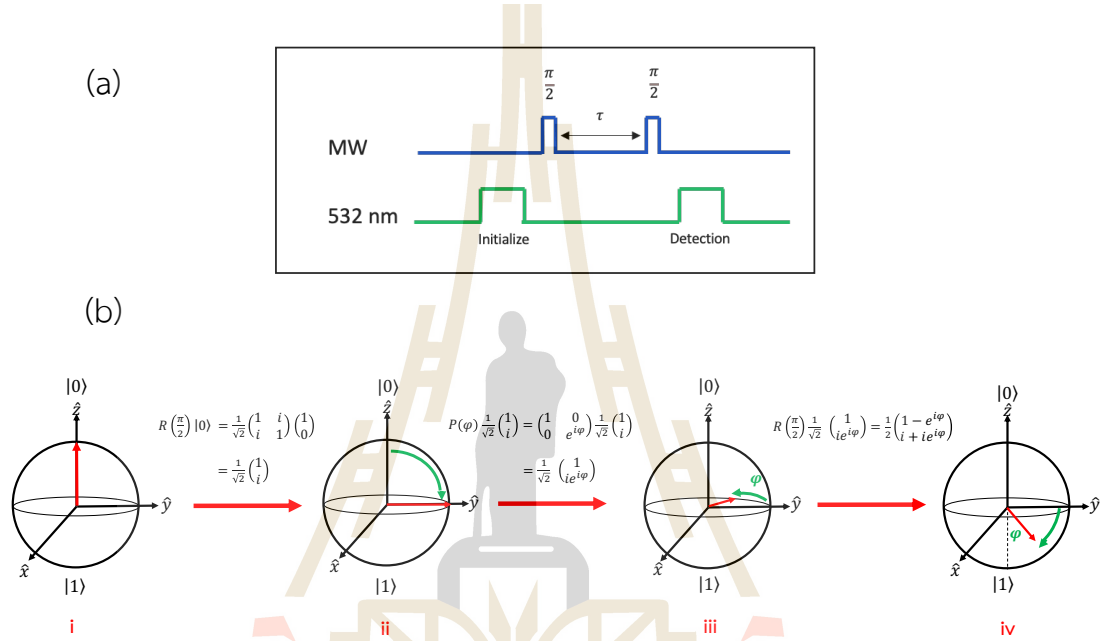


**Figure 2.6** (a). Pulse sequence for the Ramsey experiment. (b). This picture shows the process and the state evolution of the qubit in the Ramsey experiment. (i) Prepare initial state in the north pole of Bloch sphere. (ii) Apply  $\frac{\pi}{2}$  pulse to rotate the state into the equator. (iii) The qubit freely rotates on x-y plane. (iv) apply  $\frac{\pi}{2}$  pulse again.

The Ramsey process shown in figure 2.6(a) start by initializing state at the north pole of the Bloch sphere (state  $|0\rangle$ ) and then apply  $\frac{\pi}{2}$  pulse whose function is to rotate the state around the x or y axis with angle  $\theta = \frac{\pi}{2}$ . The state after this step will be moved to the equator (superposition state between state  $|0\rangle$  and state  $|1\rangle$ ). According to Section 2.4.1, if we apply the off-resonance frequency ( $\omega \neq \omega_0$ ) to the system, this affects the qubit state slightly, with phase  $\varphi$  changing with detuning frequency  $\frac{d\varphi}{dt} = \delta = (\omega - \omega_0)$ . After allowing the qubit to evolve with time  $\tau$ , this process provides the



phase different  $\varphi = \delta \cdot \tau$  between state  $|0\rangle$  and state  $|1\rangle$ . After that, apply  $\frac{\pi}{2}$  pulse again to rotate the state into the south pole (state  $|1\rangle$ ). After that, we measure the intensity of the light that is emitted from the NV-center to find the population of the qubit final state. The result from this experiment shows the dephasing behavior that including noise from the spin bath and gives us the ensemble dephasing time  $T_2^*$ . The evolution of a qubit state throughout this process is shown in figure 2.6(b).

### 2.4.3 Spin echo

The spin echo is a technique proposed in 1950 by Erwin Hahn to reduce the decoherence of quantum systems (Hahn, 1950). By employing a pulse sequence protocol to cancel out the effect of unwanted spin bath signals as shown in figure 2.7(a). The spin echo process begins with the initialization of the qubit to state  $|0\rangle$ . Then, applying  $\frac{\pi}{2}$  pulse to project the qubit onto the equator of the Bloch sphere or project the system into the superposition state  $\frac{1}{\sqrt{2}}(|0\rangle + i|1\rangle)$ . Due to the effect of the external magnetic field, if the system contains a large number of spins, each spin will precess at its own detuning  $\delta$ . After waiting for time  $\tau$  it will make a phase different between state  $|0\rangle$  and state  $|1\rangle$ . Then, we apply a  $\pi$  pulse to flip all the spins in the opposite direction of the Bloch sphere. If we wait the exact time  $\tau' = \tau$ , all spins will refocus at the same point and all of unwanted signals are removed from the system. Finally, we will apply a  $\frac{\pi}{2}$  pulse again and measure the spin population. This process provides us the dephasing time that subtract noise from the environment  $T_2$ . The visualization of this process on the Bloch sphere is shown in figure 2.7(b).

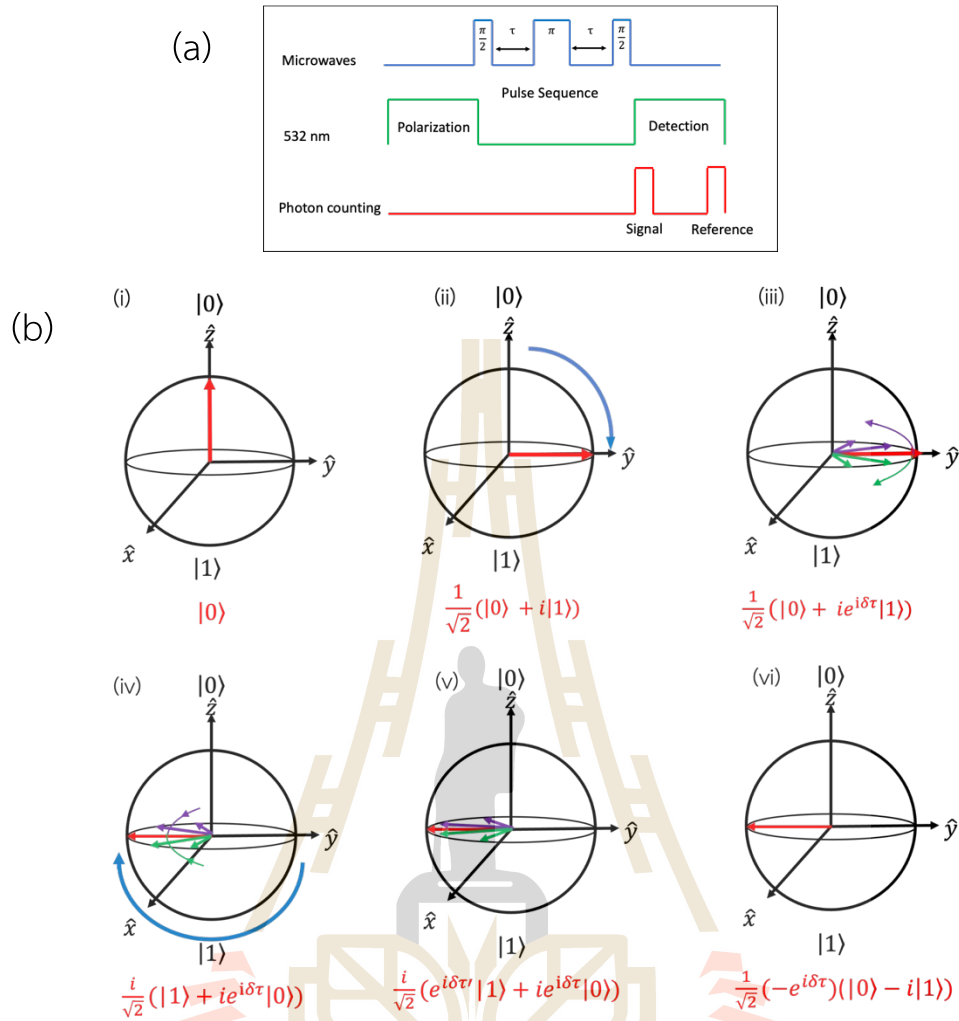
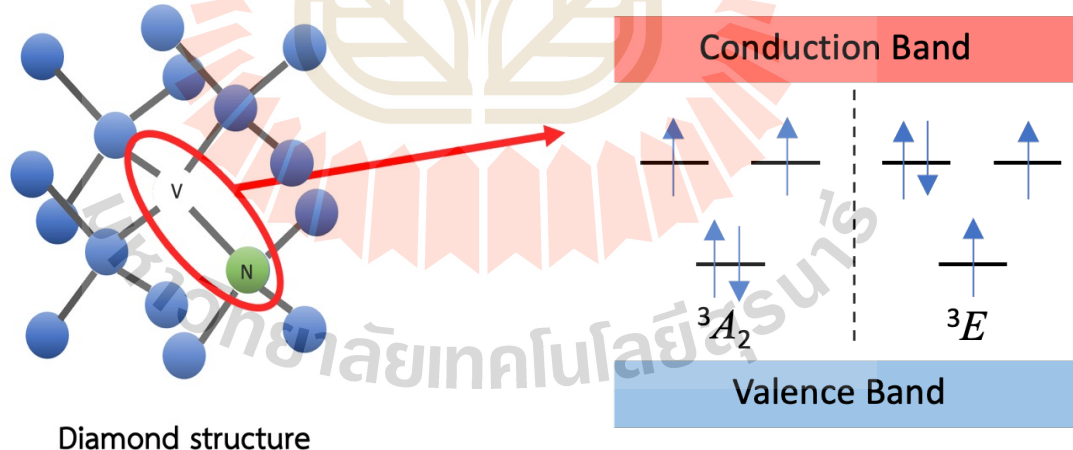


**Figure 2.7** (a) Pulse diagram for spin echo experiment. (b) The process and the state evolution of the qubit in the spin echo process. (i) The qubit was prepared in the state  $|0\rangle$ . (ii) Then, apply  $\frac{\pi}{2}$  pulse to project the qubit onto the equator of the Bloch sphere. (iii) Due to the effect of the external magnetic field. After waiting for time  $\tau$ , the spin will precess and causing the phase different between state  $|0\rangle$  and  $|1\rangle$  with related to factor  $\delta \cdot \tau$ . (iv) we apply a  $\pi$  pulse to flip all the spins in the opposite direction of the Bloch sphere. (v) Waiting for time  $\tau'$ , all the spin will refocus at the same point. (vi) After waiting for time  $\tau' = \tau$  all of the unwanted effects will be removed, and the final state will recombine at the same point.

## 2.5 Nitrogen-vacancy center

The nitrogen-vacancy (NV) center in diamonds is a defect in structure that is caused by replacing two of the carbon atoms in the diamond structure with a nitrogen atom and an adjacent vacancy. The interested type of the NV center is the negatively charge NV center or  $\text{NV}^-$  which is formed by six electrons, three from carbon atom, two from nitrogen atom and one from environment as shown in figure 2.8. The  $\text{NV}^-$  ground state is a spin triplet state which can be manipulated by using optical and microwave techniques to obtain the zero-phonon line at wavelength 637 nm (Gruber, Drabenstedt et al., 1997).

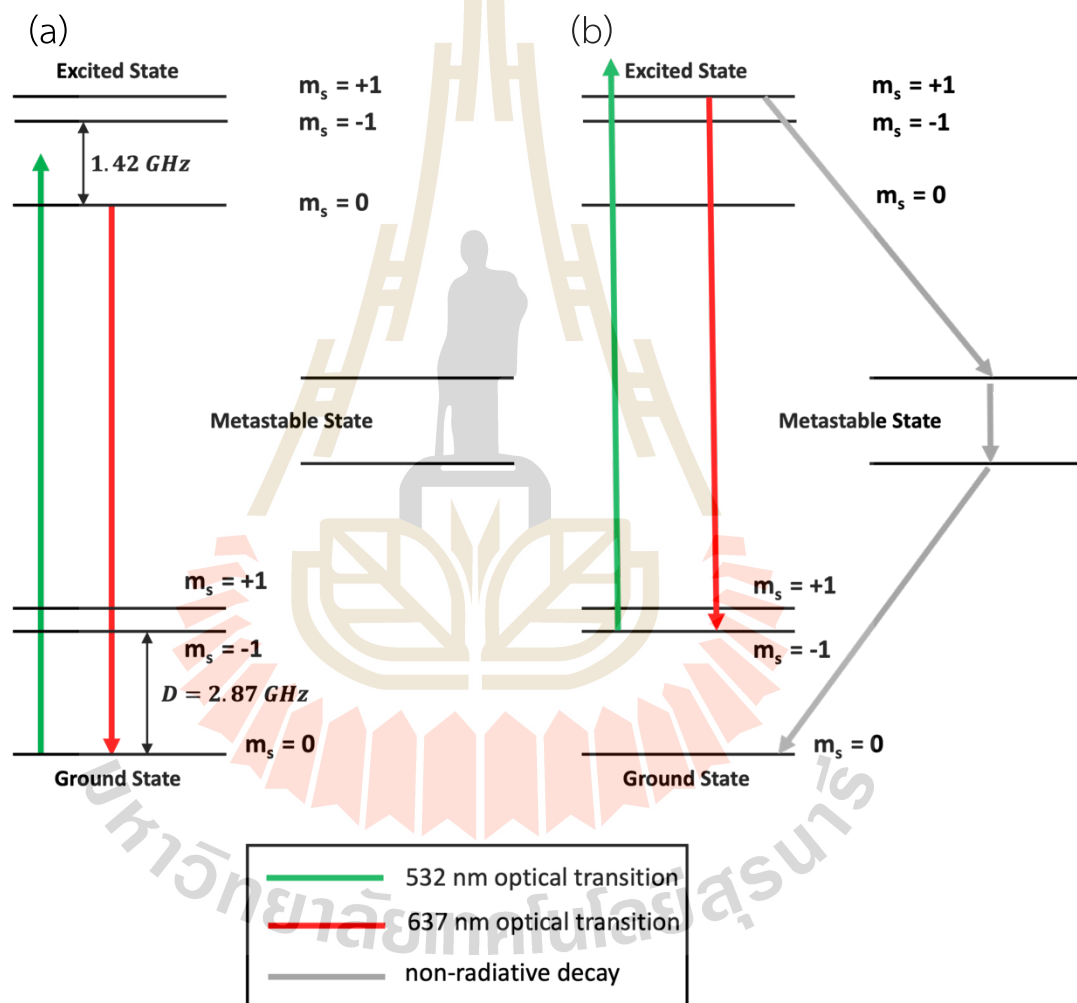
Due to optical and spin properties of the NV center, it can be used in several quantum technology such as qubits in quantum computing (Childress et al., 2013), nanoscale magnetometers (Hong, Grinolds et al. 2013), and probing several parameters such as electric field (Jamonneau et al., 2016), material strain (Grazioso et al., 2013) and temperature (Toyli et al., 2013) with high sensitivity.



**Figure 2.8** This picture shows  $\text{NV}^-$  system that is caused by the substitution of one carbon atom with a nitrogen atom. The three unpair electrons are occupied in the  $^3A_2$  ground state while they are localized on these carbon atoms and the nitrogen atom in the  $^3E$  excited state.

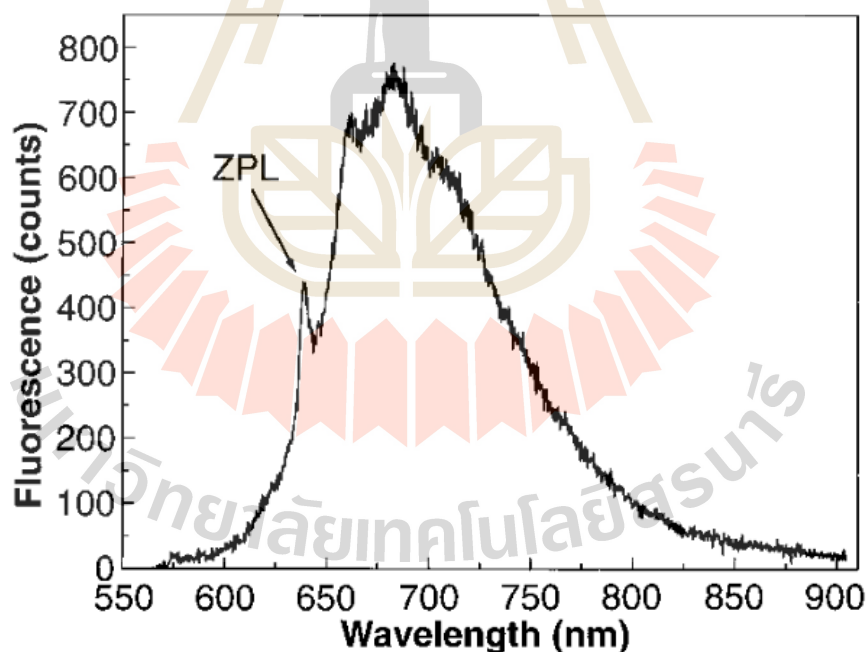
### 2.5.1 Energy Diagram of the NV center

Figure 2.9 shows the energy diagram for the NV center which has a triplet state at the ground state and an excited state with  $m_s = 0$  and degenerate state  $m_s = \pm 1$ . We can excite the electron in the ground state by using an off-resonant green laser which has wavelength of 532 nm. and then the NV will emit the fluorescence via the red light which has the zero-phonon line at 637 nm as shown in figure 2.10.



**Figure 2.9** The energy level diagram for the NV center. (a). Electron start in spin  $m_s = 0$ , after it was excited by using green laser, it will emit the red fluorescence. (b). For electron starts in spin  $m_s = \pm 1$ , the electrons in this case have two channels to go through, one with the same part as (a) and emitting the same fluorescence and one will go to the metastable state with the non-radiative decay.

By probing the NV in the excitation process with microwave signal at 2.87 GHz that corresponds with a zero-field splitting, some population of the electron in the ground state with  $m_s = 0$  will go to the degeneracy state  $m_s = \pm 1$ . For this part, after exciting the electron, the electron can go to state  $m_s = \pm 1$  of the excited state. The electrons in this case have two channels to go through, one with the same path as mentioned before and emitting the same fluorescence and one will go to the metastable state with max probability around 60 – 80% (Childress et al., 2006, Manson et al., 2006, Robledo et al., 2011) with the non-radiative decay with a long lifetime  $\sim 300$  ns compared to lifetime in the general path ( $\sim 20$  ns) (Storteboom et al., 2015). From this property, the intensity of the light that is emitted from the NV-center in state  $m_s = 0$  and  $m_s = \pm 1$  are different as shown in figure 2.11. We can distinguish the spin state of the electron in the NV center by considering the photon counts rate.



**Figure 2.10** This graph shows the fluorescence emission from the NV center. The NV center release a light spectrum in the 600 – 800 nm range with a zero-phonon line at 637 nm (Gruber et al., 1997).

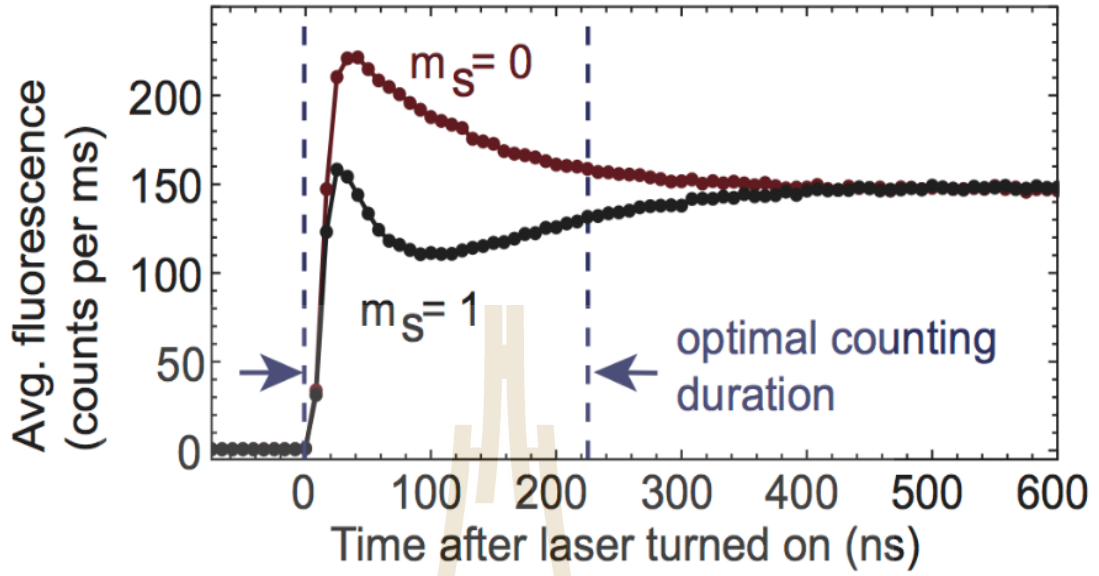


**Figure 2.11** This graph shows that photoluminescence is dependent on the number of spin states, with spin state  $m_s = 0$  providing a higher initial fluorescence rate than spin state  $m_s = 1$ . Therefore, we can use this phenomenon to determine the electron's spin state of the NV center (Gupta et al., 2016).

### 2.5.2 NV center Hamiltonian

To study the properties of the NV center, we can consider the Hamiltonian as shown below.

$$H = DS_z^2 + \gamma_e \vec{B} \cdot \vec{S} + \sum_k (\vec{S} \cdot A_k \cdot \vec{I}_k + \gamma_k \vec{B} \cdot \vec{I}_k) \quad (9)$$

The first term of the Hamiltonian describes zero field splitting, where  $D = 2.87 \text{ GHz}$  is the parameter for zero-field splitting and  $S_z$  is the spin operation along the  $z$  axis (NV axis). The second term describes the Zeeman-splitting between the degeneracy states  $m_s = -1$  and  $m_s = +1$ . By applying an external magnetic field, the energy of these two states will separate, based on the electronic gyromagnetic ratio  $\gamma_e = 2.802 \text{ MHz/Gauss}$ . And the last two terms describe the effect of the nuclear spin in the system, the first term is the hyperfine interaction term, and the second term is the Zeeman splitting term, where the hyperfine tensor associated with each coupling is given by  $A_k$ , and the gyromagnetic ratio of each nuclear spin is given by  $\gamma_k$ .



Figure 2.12 shows the energy splitting of the state  $m_s = -1$  and  $m_s = +1$  from state  $m_s = 0$ . For absence of the external magnetic field, the state  $m_s = \pm 1$  have equal energy different from  $m_s = 0$  at 2.87 GHz. And for increasing the magnitude of the magnetic field along the NV axis, they will split from each other with factor  $2\gamma_e B_z$ .

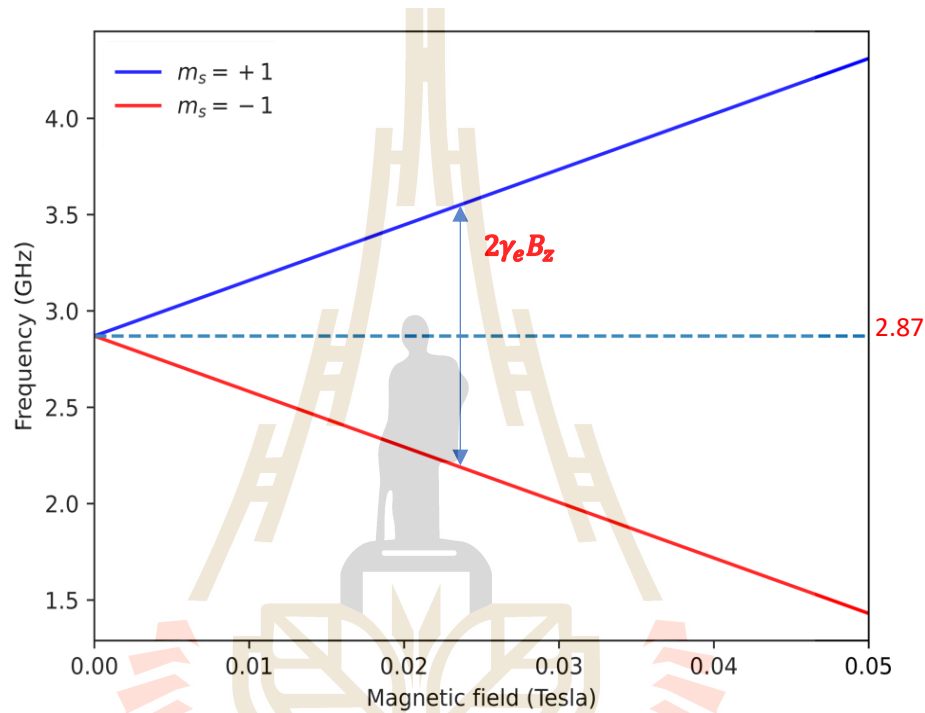


**Figure 2.12** This graph shows the Zeeman-splitting effect on the electron in the NV center. The energy (in terms of frequency) of each spin state will split from each other depending on the magnitude of an external magnetic field.

### 2.5.3 The hyperfine coupling between $^{13}\text{C}$ and the NV center

In the NV center system, it is surrounded with the carbon atom, around 98.9% of the spinless  $^{12}\text{C}$  and 1.1% of the  $^{13}\text{C}$ . The  $^{13}\text{C}$  have spin  $\frac{1}{2}$ , which can cause the strong hyperfine interaction with the nearby electron from the NV center. So, we can use the coupling between them to control a quantum register.

For the quantum register that is manipulated from nuclear spins of the carbon atom it have a longer coherence time than electron spin due to the ratio between the gyromagnetic ratio of the electron spin and nuclear spin. We can use two control pulses to operate electron and nuclear spin as a quantum register. The energy diagram of the electron spin and nuclear spin are shown in figure 2.13.

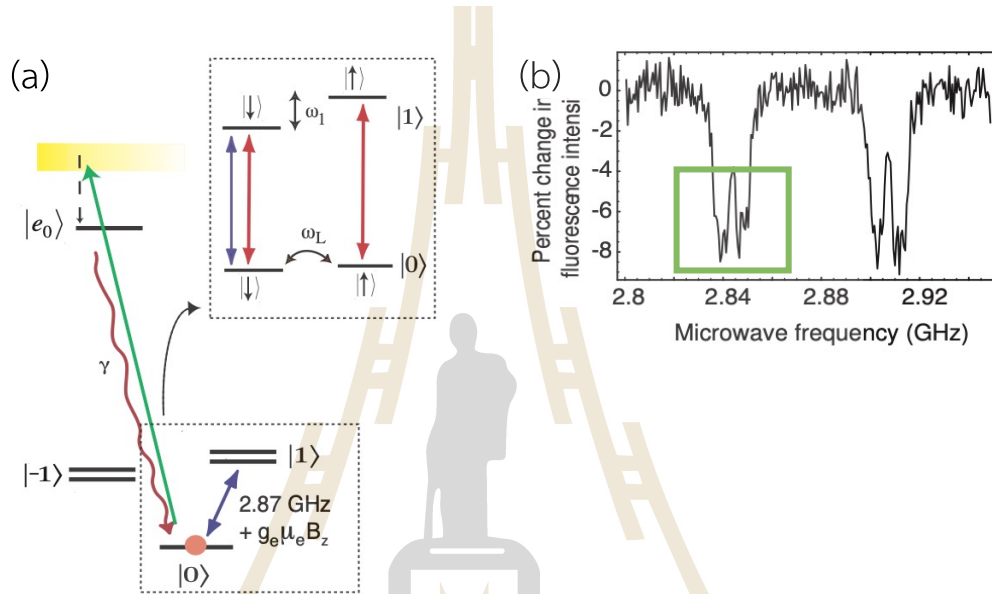


**Figure 2.13** (a) The energy diagram for the coupling between the electron spin and nuclear spin from  $^{13}\text{C}$ . (b) This is the ODMR result that show the transition of the  $^{13}\text{C}$ . The green box show the splitting between the spin  $|\downarrow\rangle$  and  $|\uparrow\rangle$  of  $^{13}\text{C}$  the nuclear spin (Dutt et al., 2007).

The electron in the states  $m_s = 0$  and  $m_s = 1$  is used as the first qubit, while the nuclear spin with spin up and spin down is used as the second qubit. In the  $m_s = 0$ , the hyperfine interaction between electron spin and nuclear spin cannot be seen. If we apply a magnetic field perpendicular to the nuclear spin axis, the nuclear spin will flip between spin up and spin down with the Larmor frequency  $\omega_L$ . In the  $m_s = 1$  manifold, the hyperfine interaction causes the energy shift between spin up and spin down of the nuclear spin with a frequency  $\omega_1 = A_{zz}$  in range up to 20 MHz in both

low and high magnetic field (<50 G and 510 G) (Smeltzer et al., 2011). This energy diagram can be used to control the quantum register system.

The energy diagram for the coupling between the electron spin of the NV center and the nuclear spin of  $^{13}\text{C}$  is useful as a quantum register. The set of the hyperfine strength between NV electron spin and the different locations of  $^{13}\text{C}$  nuclear spin are shown in table 2.2 with the visualization in figure 2.14. From the table, all frequencies are given in MHz, numbers in parentheses give error in the last digit.

**Table 2.2** The observed and theoretical hyperfine splitting ( $A_{hfs}$ ) of  $^{13}\text{C}$  nuclear spin in different lattice sites at low magnetic field (<50 G).

Lattice site	Distance to site (Angstrom)	Sites	$A_{hfs}$ theory	$A_{hfs}$ experiment
A	3.89	6	14.8(1)	13.72(3)
B	3.90	3	13.9(1)	12.78(1)
C	2.52	3	-7.5(1)	-8.92(3)
D	2.50	5	-5.7(2)	-6.52(4)
E, F	2.93, 2.96	6, 3	4.6(1), 4.67(4)	4.2(1)
G, H	5.05, 5.05	6, 3	2.63(7), 2.27(4)	2.4(3)

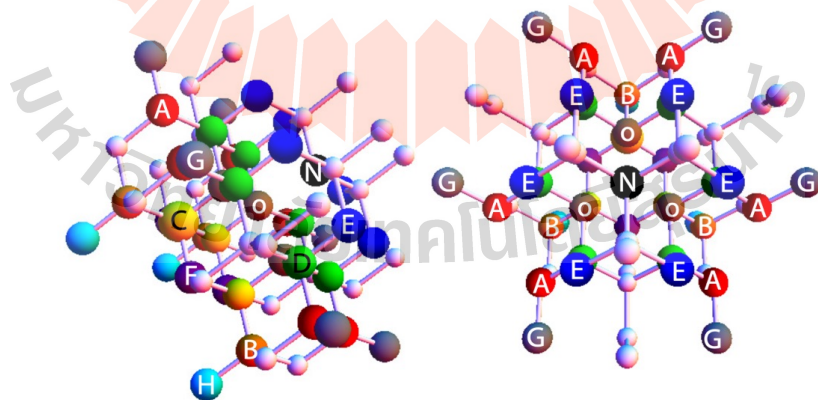


**Figure 2.14** Visual representation showcasing the geometry of the NV defect from two perspectives. Lattice sites hosting proximal  $^{13}\text{C}$  nuclear spins, denoted as outlined on Table 2.2. The nitrogen sites are marked as “N”, while sites labeled “O” represent the nearest neighbors to the vacancy ( $A_{hfs} = 130$  MHz) (Smeltzer et al., 2011).

## CHAPTER III

### RESEARCH METHODOLOGY

First, we introduce the properties of the NV center sample that used in our work. We show our setup, includes the AOM setup, confocal setup and the microwave instrument setup. We started our worked by using a confocal microscope to observe the fluorescence from the NV center. After addressing the location of the NV center, microwave sequences are applied to NV sample to perform quantum process to manipulate our system.

#### 3.1 NV center Sample

We used single-crystal electronic (ELSC) grade diamond with a low NV concentration (less than 0.03 ppb) purchased from Element Six Ltd. The diamond plate size is 2 x 2 mm with a thickness of 0.5 mm. The sample was implanted with  $^{15}\text{N}$  with an energy of 30 keV and annealed to form NV centers (Sangtawesin et al., 2019). The sample is attached to the PCB board fabricated with a coplanar waveguide, which has a characteristic impedance close to 50 ohms. A 25  $\mu\text{m}$  aluminum wire was stretched above the sample for carrying the microwave signal to the sample. Magnetic field  $\mathbf{B}$  was applied to the sample with a permanent magnet that can be adjusted to tune the magnetic field orientation along one of the NV center axes.

#### 3.2 Acousto-Optic Modulator (AOM) setup

AOM is a device used for controlling intensity of laser beam. It consists of a piezoelectric transducer attached to a crystal material. When RF signal (electric current) is applied to the transducer, it will vibrate because of piezoelectricity, and generate acoustic wave travelling in the crystal. Due to photo-elastic effect, the moving plane of transducer produces periodic change in refractive index in the crystal which is similar

to a diffraction grating. When light is coming to this grating in AOM, the light is diffracted into several orders and interference pattern occurs at the output. From this property, we choose the first-order beam from the AOM to use in our optical setup.

The setup diagram of the AOM is shown in figure 3.1(a). We use a convex lens with a focal length of 150 mm to focus a beam from the 532-nm laser into the AOM (G&H AOMO 3080-120). The time trigger of the AOM is control by using a pulse blaster (Spincore Technologies PulseBlaster ESR-PRO500). Moreover, two mirrors are used for easily align the path of the green laser. Finally, we use another convex lens with a focal length of 150 mm to collimate the beam after passthrough the AOM focus on a single-mode fiber coupler (Thorlabs PAF2P-A7A), which connects to a confocal microscope setup as shown in the next section. The results from turn on and turn off the AOM system are shown in figure 3.1(b).

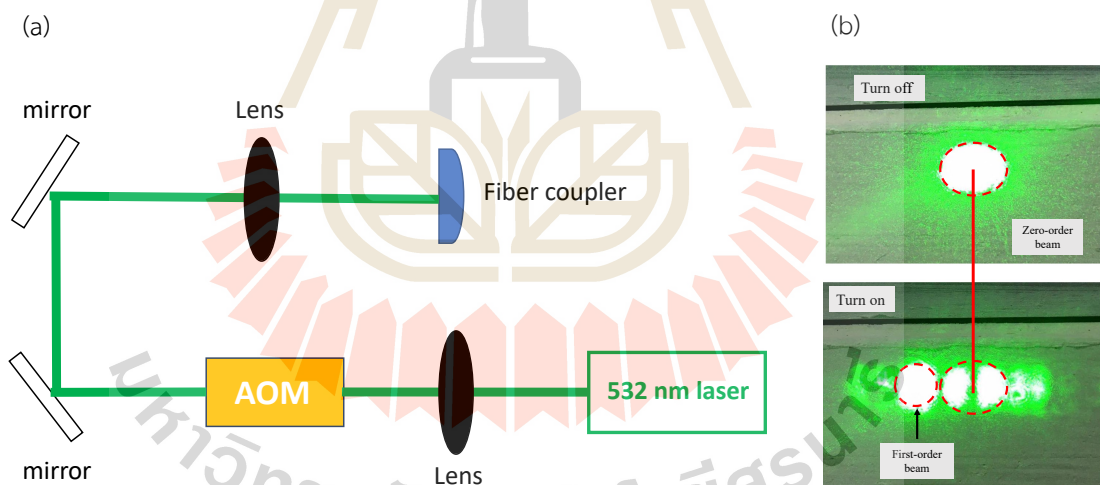


**Figure 3.1** (a) Diagram of the AOM setup. (b) The outputs of the green laser when turn off (left) and turn on (right) the AOM.

### 3.3 Single-Photon Confocal microscope

The confocal microscope obtains a high imaging resolution by using the focal point of the light to create an image and by filtering out noise from other sources. The

confocal can scan images in three dimensions, which is useful for studying materials that emit fluorescence, such as biological (Hepler and Gunning, 1998) and chemical (Nie, Chiu et al., 1994), and the NV center in particular. The schematic for the confocal setup is shown in figure 3.2.

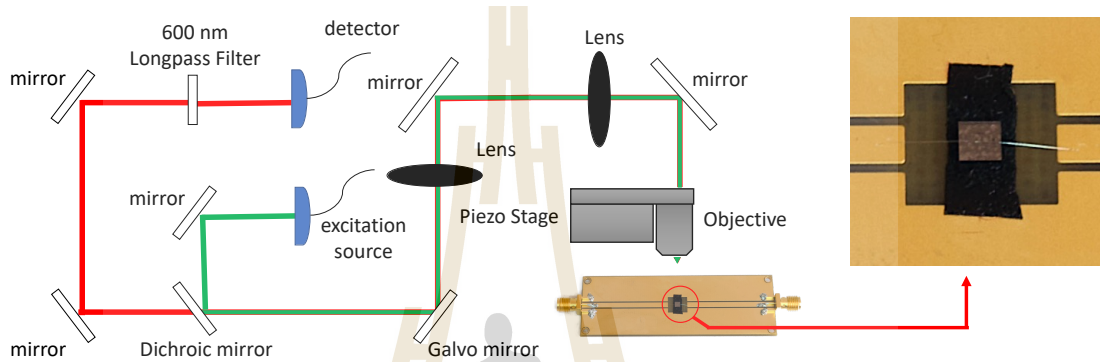


**Figure 3.2** Diagram of the confocal microscope setup. The NV sample is attached to the PCB board based on the coplanar waveguide design, and a 25  $\mu\text{m}$  aluminum wire above the sample is used to carry the microwave signal to the sample.

We placed the NV sample on the sample mount in the setup. The excitation source is a green laser with a wavelength of 532 nm (Coherent OBIS 532) which is aligned to the sample by following the green path shown in the image. The mirrors in the diagram (Thorlabs BB1-E02) are used to align the laser beam. We use the galvo mirror (Thorlabs GVS 212/M) which can adjust the green laser to scan the sample in two directions (x-y plane). After passing the galvo, the beam will be focused on the sample by using lenses L1 and L2 with a focal length of 150 mm (Edmund Optics 49-390), at the position in front of the sample, the beam was focused on the sample by installing the 100x objective lens (Olympus MPLFLN100X). We install the sample on the piezo stage to make this system capable of scanning in the z-direction and fine-focusing a confocal image. When the NV is excited by the green laser, it will emit photons (release fluorescence) with a spectrum from 600 - 800 nm. The photon will



follow the same path as the green laser to the dichroic mirror (Thorlabs DMLP567) that can transmit 637 nm light and reflect 532 nm laser. The photon will pass through the dichroic to fiber launch lens (Olympus MPLFLN10X) that connected with a fiber optics (Thorlabs - P1-630A-FC-2) then, go to an avalanche photodiode detector (APD). A Long-pass filter (Thorlabs FELH600) was installed in front of the APD to prevent the excitation beam from entering the detector. The detector will show the signals in terms of photon counts. The confocal microscope setup in our laboratory is shown in figure 3.3.

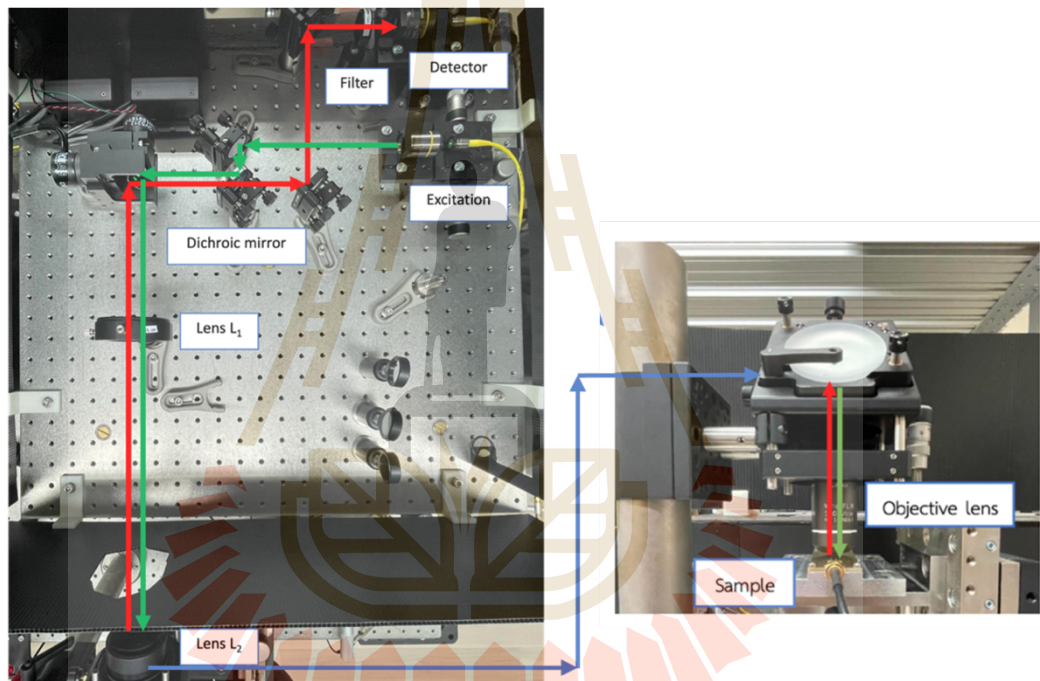


**Figure 3.3** Picture of the confocal microscope setup. The green line shows path for the excitation source and the red line shows path for the light emission from the sample.

### 3.4 Microwave-control system

In the metrology and computation fields of quantum physics that using NV as a key material, we use a microwave signal to manipulate the state of electron spin of the NV center. The schematic of the microwave control system is shown in figure 3.4.



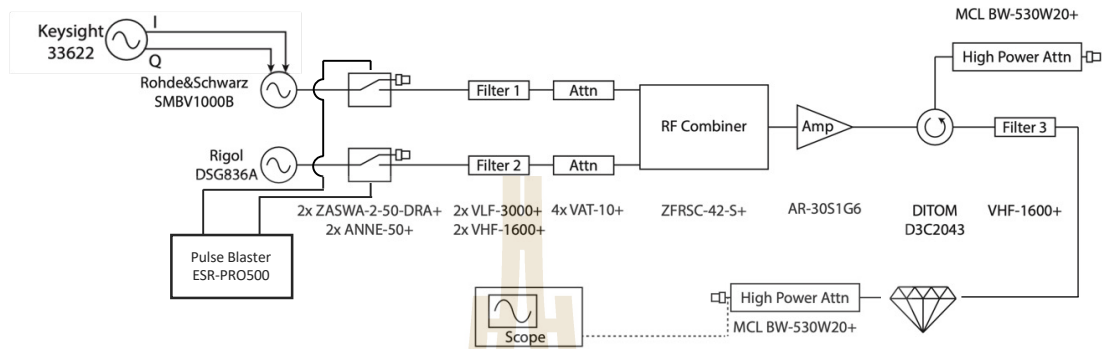


**Figure 3.4** Diagram for the microwave control system.

We use two sources of the microwave generator (RIGOL DSG836A and Rohde&Schwarz SMBV100B). The phase of SMBV100B is controlled by using an external I-Q modulator (Keysight 33622A). The generated signal enters through a microwave switch circuit (ZASWA-2-50DRA+), powered by a  $\pm 5$  V power supply, to manipulate the signals. We use a pulse pattern generator (Spincore Technologies PulseBlaster ESR-PRO500), which outputs transistor-transistor logic (TTL) signals to control the timing trigger of the microwave signals. We block one of the RF OUT (1) channels by using a terminator (MCL ANNE-50+) and release the microwave signals to pass through another RF OUT (2) channel. Before the signals go to the amplifier (ZHL-15W-422-5+), we use two filters, a high-pass filter (VHF-1600+) and a low-pass filter (LF-3000+) after the two sources of the microwave to eliminate higher and lower frequency harmonics from switching. we used two sets of -3dB attenuator (VAT-3+) and -10 dB attenuator (VAT-10+) to reduce the signal to not exceed the limitation of the amplifier (not exceed +7 dB), then combine the signals from each source by using an RF combiner (ZFRSC-42-S+). Afterward, the attenuated signal will go to the circulator (DITOM D3C2040) to protect the reflected signal from the sample from going back to the amplifier. The reflected signal from the last port of the circulator is blocked by the terminator (MCL BW-530W20+). Finally, before passing the signals to the sample, we used a high-pass

filter (VHF-1600+) to filter the amplifier noise and monitor the signal via the oscilloscope.

Figure 3.5 shows the microwave signal monitor from the oscilloscope (Keysight MSOX6004A). The power and frequency of the signal are set at 0 dBm and 2.0 GHz from the original source. From the result, the amplitude of the microwave signal is reduced around 50% after passing the NV center sample.

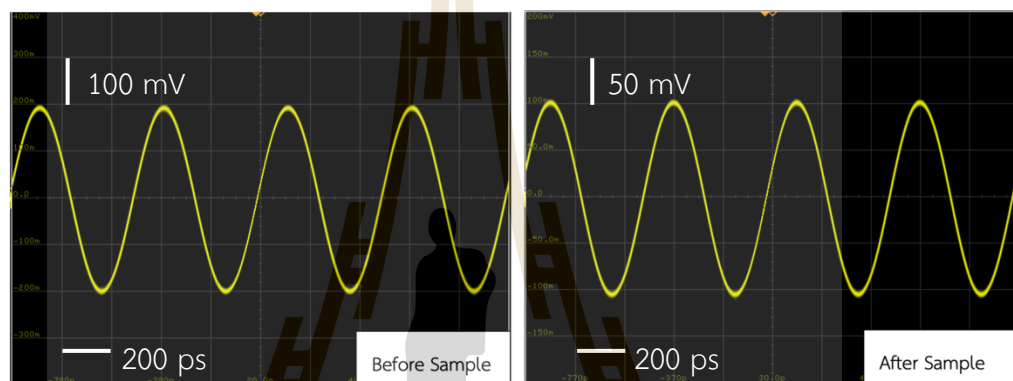


**Figure 3.5** The microwave signal before and after passing the NV sample.

### 3.5 Pulse experiment for NV center experiment.

As mentioned in section 2.5.1, we can polarize and read out the electronic spin of an NV center by using the optical excitation. By adjusting a microwave field with frequency matching with the transitions of the spin, we can easily control its manipulation as well. The whole picture for access the controlling of the NV center is shown in the figure 3.6(b). We apply the external magnetic field to obtain the spin state that we focused, then manipulate the spin state with the microwave signal. During this process, one excites the ground state population of the NV to the excited state, then read out the signal of the system through fluorescence photon counting. Excitation of the NV center with these ingredients provide a straightforward means to prepare, manipulate, and measure a single electron spin in the solid state at room temperature (Jelezko et al., 2002).

The scheme for the NV center pulsed experiment consists of three important parts, as shown in figure 3.6(b). All experiment start with the polarization of electron spin and end with the measurement of electron spin state, both facilitated by 532nm excitation. Throughout the process, various microwave pulse sequences can be employed to manipulate the electron spin, the data is collected in term of the photon counts. We measure the PL immediately after any operation of the microwave pulse sequence as a signal data, and after waiting until the electron state was polarized we measure the PL again as a reference signal. The PL data is shown in term of the normalized data, which is calculated from the equation as shown below.

$$PL = 1 - \frac{|\text{signal} - \text{reference}|}{\text{reference}} \quad (10)$$

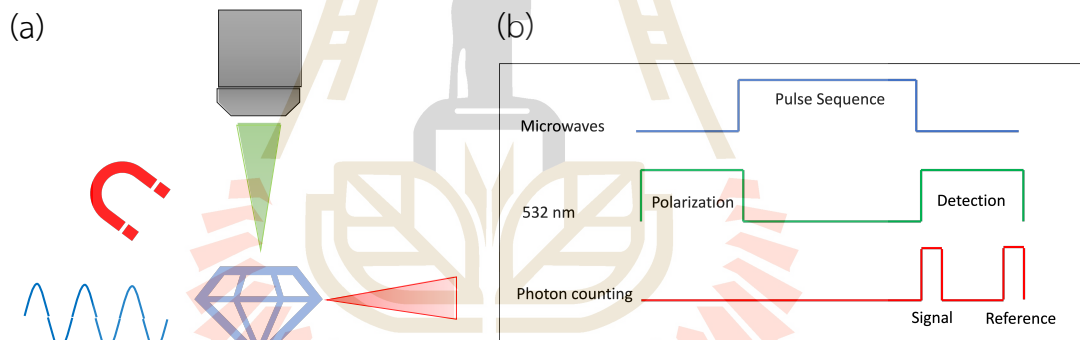


**Figure 3.6** (a) The whole picture for the NV center experiment. (b) The diagram for the NV center pulsed experiment.

## CHAPTER IV

### RESULTS AND DISCUSSION

This chapter presents the results and the discussion. The contents consist of a single NV center picture taken from the confocal microscope. The characterization of the coupled electron in NV center and the  $^{13}\text{C}$  nuclear spin data are shown in this chapter, including a pulsed-ODMR experiment and the Rabi oscillations for weak and strong transitions of that system. Moreover, we achieve to observe and control the  $^{13}\text{C}$  nuclear spin, which shows the free precession data with the dephasing and the Ramsey experiment of those in spin  $m_s = -1$  manifold. Furthermore, we perform the  $\pi$  pulse on the  $^{13}\text{C}$  nuclear spin during the free precession by using the hyperfine effect, which can flip the nuclear spin state faster than the bare free precession. Finally, we show the non-perfect polarization of the nuclear spin projection in the nuclear Ramsey experiment.

#### 4.1 The single NV picture from the confocal microscope

The NV center picture that is scanned from the confocal microscope is shown in figure 4.1. the left picture shows a scanned NV center over an  $80 \times 80 \mu\text{m}^2$  area. the dash line is the aluminum wire observed under the confocal microscope. The right picture shows a scanned NV center in  $10 \times 10 \mu\text{m}^2$  area. Each bright spot in the picture is a single NV center. We choose the NV in the white circle, which is close to aluminum wire to obtain large field amplitudes of the AC magnetic field signal from the microwave source.

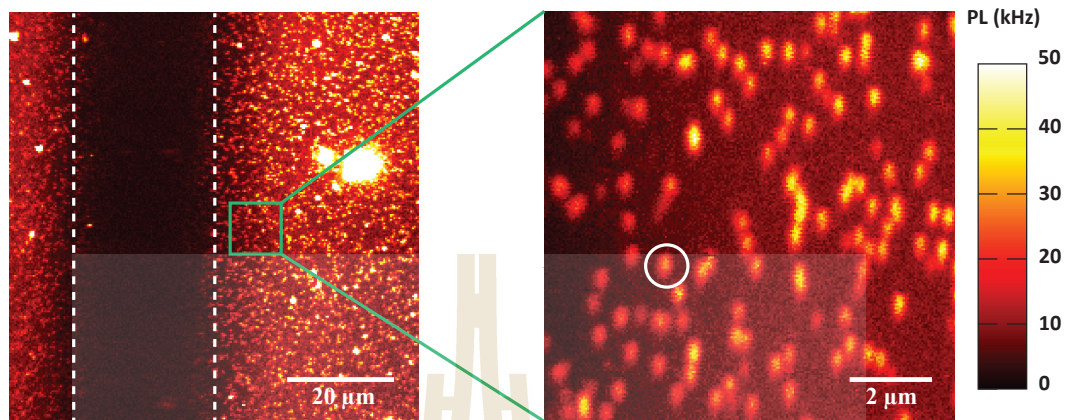


**Figure 4.1** The picture of the diamond surface that was taken by the confocal microscope with the scanning area  $80 \times 80 \mu\text{m}^2$  (left) and  $10 \times 10 \mu\text{m}^2$  (right); the dash line is the aluminum wire observed under the confocal microscope.

## 4.2 Optically detected magnetic resonance (ODMR)

We used optically detected magnetic resonance (ODMR) to accomplish ground state spectroscopy on a single NV center includes zero field, Zeeman splitting, and the hyperfine splitting transitions.

### 4.2.1 Zero field signal

In the experiment, a microwave field is applied to the sample, then the frequency is varied, and the photoluminescence (PL) is observed from the sample as shown in figure 4.2(a). The NV center is polarized by a 532-nm excitation laser to the  $m_s = 0$  state and its PL is highest when microwave frequency is tuned around the electron spin transitions, it will generate transitions between the  $m_s = 0$  and  $m_s = \pm 1$  states, repopulating the spin configuration of the NV, The PL will drop as the frequency gets closer to resonance (2.87 GHz) because the  $m_s = \pm 1$  spin states can non-radiatively decay into the shelving state. As a result, we obtained the dip from the signal as shown in figure 4.2(b).

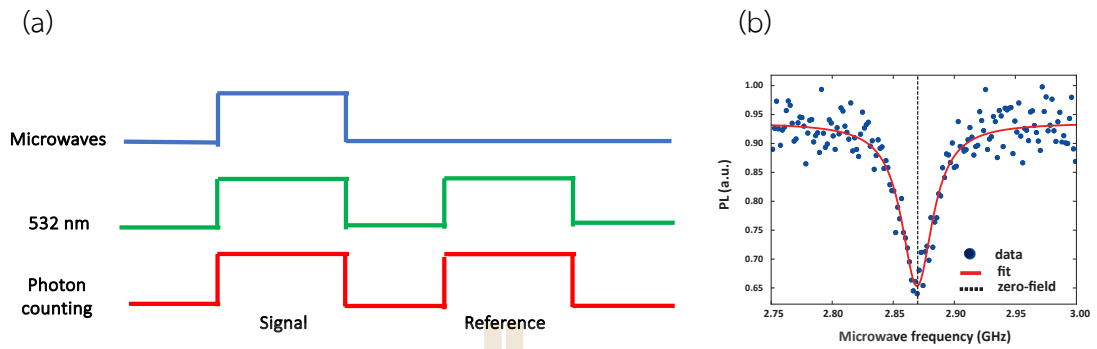


**Figure 4.2** (a) A pulse sequence for ODMR experiment. (b) Zero-field splitting signal from our NV sample, this shows the dip appears at frequency 2.87 GHz.

#### 4.2.2 Zeeman-splitting signal

The pulse sequence to observe this phenomenon is the same as figure 4.2(a). Applying an external magnetic field to the sample causes Zeeman splitting of the  $m_s = \pm 1$  states, breaking the degeneracy. The Zeeman splitting between the  $m_s = -1$  and  $m_s = +1$  states correspond to the distance between the two transition frequencies. In an experiment, this is accomplished by installing a permanent magnet close to the sample as shown in figure 4.3(a), then varying its location by using a rotational stage, which can adjust the azimuthal and polar angle to fine-tune the magnitude and the direction of the magnetic field. The NV axis is located at faces  $[111]$ ,  $[\bar{1}\bar{1}\bar{1}]$ ,  $[1\bar{1}\bar{1}]$ , and  $[\bar{1}11]$ . For the matching direction of the magnetic field and the NV axis, the splitting between two transitions will be largest. Measuring this signal is very important because we can use one of the two transitions as a qubit.

From the graph in figure 4.3(b), we apply a magnetic field  $B_z = 46$  G to the NV center. There are two dips occur in the graph at frequencies 2.746 GHz and 2.998 GHz. The first dip results from the transition of electron from  $m_s = 0$  to  $m_s = -1$  and the second dip results from the transition of electron from  $m_s = 0$  to  $m_s = +1$ . We can use one of the transitions as a two level system to create a qubit.



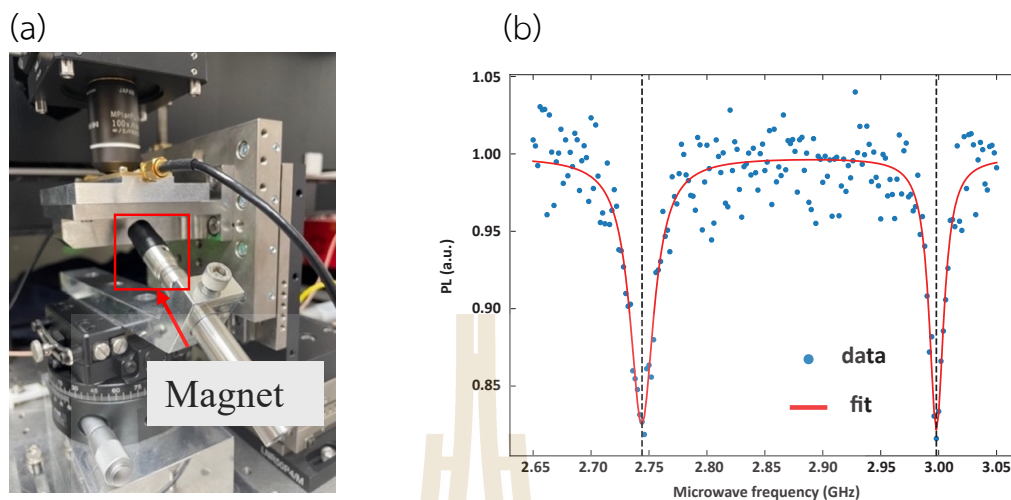


**Figure 4.3** (a) Installation of magnet into the setup. (b) Zeeman-splitting signal at magnetic field  $B_z = 46$  G. Two dips are at frequencies 2.746 GHz and 2.998 GHz.

#### 4.2.3 Hyperfine splitting signal

The hyperfine effect from the nuclear spins is much smaller compared to Zeeman splitting of the electron spin so, we need to change the pulse sequence of the experiment to the pulsed-ODMR experiment, which show in figure 4.4(a). We used the microwave with a pulse width of 1120 ns and a power of  $-14.4$  dBm for the pulsed-ODMR experiment to avoid a power broadening effect in the signal (Dréau et al., 2011). The splitting line can be observed in this protocol, but the contrast is lower than the pulse sequence in figure 4.1(a). At a magnetic field  $B_z = 46$  G, figure 4.4(b) shows 4 transitions at frequencies of 2.7399, 2.7429, 2.7464 and 2.7494 GHz, respectively. These 4 transitions include the effect of 6.5 MHz hyperfine splitting from the  $^{13}\text{C}$  nuclear spin and 3.0 MHz hyperfine splitting from  $^{15}\text{N}$ .

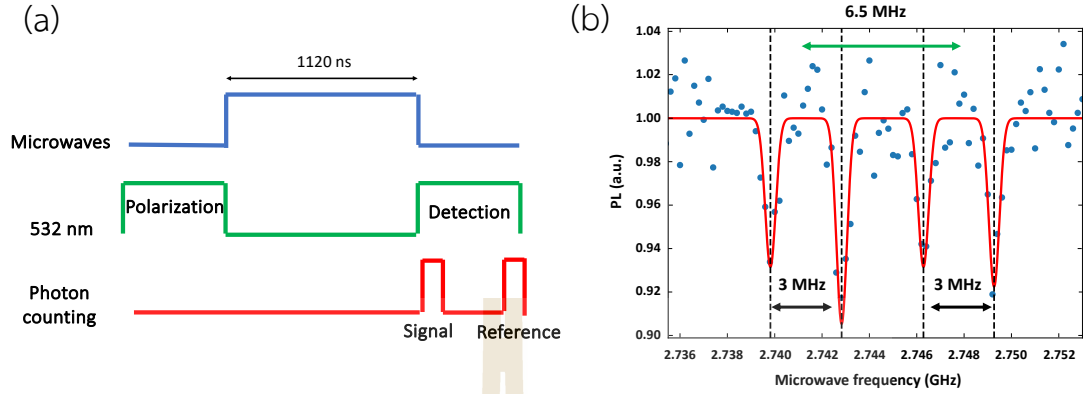


**Figure 4.4** (a) pulsed-ODMR diagram. (b) The pulsed-ODMR result at magnetic field  $B_z = 46$  G, showing the transitions at frequencies of 2.7399, 2.7429, 2.7464 and 2.7494 GHz, respectively.

### 4.3 Rabi experiment

The energy diagram of a  $^{13}\text{C}$  couple to an electron spin in the NV center is shown in figure 4.5(a). Symbols  $|0\rangle$  and  $|1\rangle$  represent the NV qubit states, where  $|1\rangle$  state can be spin  $m_s = +1$  or  $m_s = -1$  (We used  $m_s = -1$  for our work) and  $|0\rangle$  corresponds to  $m_s = 0$ . The symbols  $|\downarrow\rangle$  and  $|\uparrow\rangle$  represent the state of the  $^{13}\text{C}$  nuclear spin. In electron spin  $|0\rangle$  manifold, the nuclear spin can oscillate between the states  $|\downarrow\rangle$  and  $|\uparrow\rangle$  with a Larmor precession frequency  $\omega_L$ . In electron spin  $|1\rangle$  manifold, the hyperfine interaction introduces an energy shift between state  $|\downarrow\rangle$  and  $|\uparrow\rangle$  amounting to a frequency  $\omega_1$  (6.5 MHz for our NV). From the diagram, if we weakly drive the electronic spin state in the blue transition, with a Rabi frequency less than  $\omega_1$ , only population of the  $|0\rangle|\downarrow\rangle$  will be excited to electron spin  $|1\rangle|\downarrow\rangle$  manifold. In contrast, if we drive the system with a strong microwave pulse, with Rabi frequency greater than  $\omega_1$ , the whole population of the electron spin will be excited from electron spin  $|0\rangle$  to electron spin  $|1\rangle$  (red transitions).

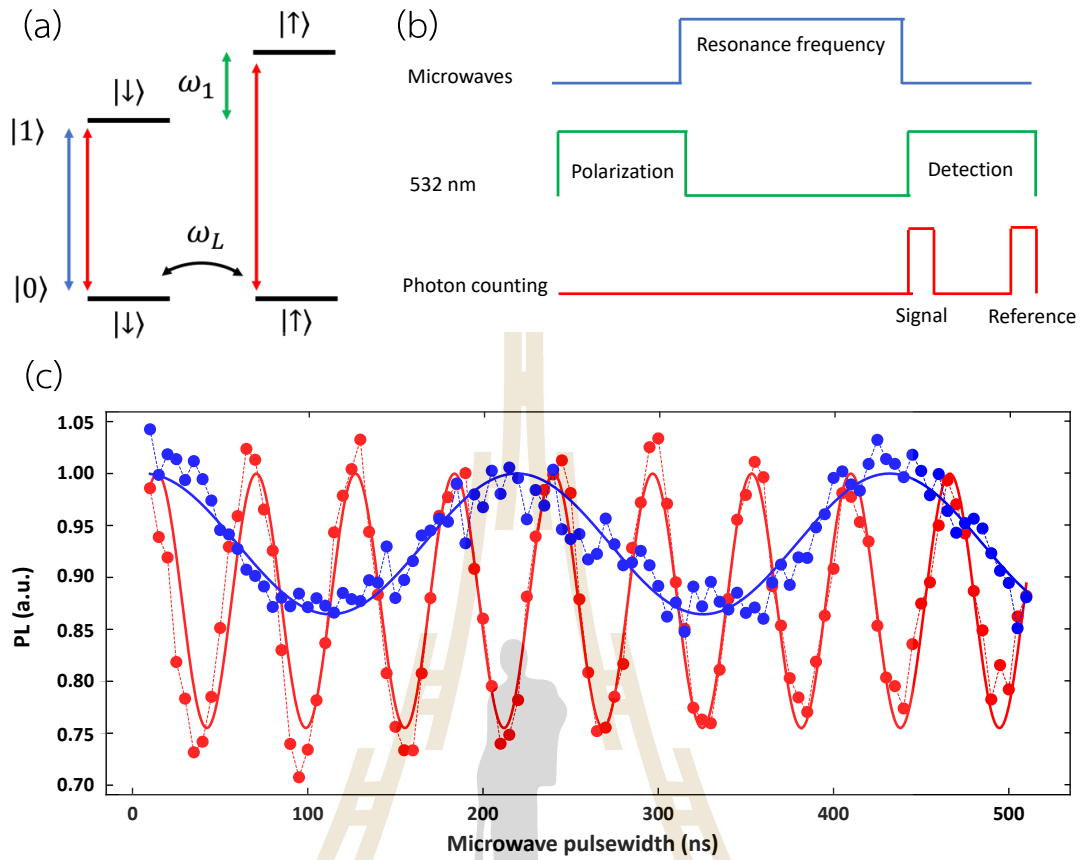


**Figure 4.5** (a) The energy diagram for the coupled NV center electron spin and nuclear spin of the  $^{13}\text{C}$ . (b) Rabi experiment pulse sequence (c) The electron Rabi oscillation data obtained by driving the resonance frequencies of the weak (blue) and strong (red) microwaves, these two have Rabi frequencies of 4.59 MHz and 17.86 MHz respectively.

To perform the Rabi experiment as the diagram shown in figure 4.5(b), by considering from the pulsed-ODMR results in figure 4.4(b). The data shows four splitting lines affect from both of hyperfine effect from the  $^{13}\text{C}$  nuclear spin and the  $^{15}\text{N}$  nuclear spin. In our work, we do not want the effect from the  $^{15}\text{N}$  so, we average the 4 frequencies from the fit to obtain the center frequency of 2.7446 GHz that is a resonance frequency of the electron Zeeman transition between state  $|0\rangle$  and  $|1\rangle$  to use as a frequency for the strong transition, which the power is set to +13.3 dBm to obtain the microwave  $\pi$  pulse duration of 30 ns . In addition, we chose the center of

the two dips from the left as the weak resonance transition frequency between state  $|0\rangle|\downarrow\rangle$  and  $|1\rangle|\downarrow\rangle$  with that is 2.7413 GHz, which the power is set to +1.3 dBm to obtain the microwave  $\pi$  pulse duration of 120 ns). Figure 4.5(c) shows the Rabi experimental data from driving the resonance of the weak (blue) and strong (red) transitions, these two have Rabi frequencies of 4.59 MHz and 17.86 MHz from the fitting, respectively. The contrast between two datasets is about of  $\frac{1}{2}$  corresponding with driving full and half of the population in the electron spin  $|0\rangle$  manifold.

#### 4.4 Nuclear free precession data

To coherently control the coupling between nuclear spin and electron spin, we follow the pulse process as shown in figure 4.6(a). Typically, the total state of the system can be written in form of the tensor product between the electron spin state and the nuclear spin state in form  $|0\rangle(\alpha|\downarrow\rangle + \beta|\uparrow\rangle)$  where  $\alpha$  and  $\beta$  are complex numbers with  $|\alpha|^2 + |\beta|^2 = 1$ . To polarize the total state of the system in state  $|0\rangle|\downarrow\rangle$ , we follow the steps from the figure 4.6(b). Starting the pulse sequence by using the green laser (532 nm) to initialize the state, then apply a weak  $\pi$  pulse to selective excite only the state  $|0\rangle|\downarrow\rangle$  to the state  $|1\rangle|\downarrow\rangle$ , so the total state will map into  $\alpha|1\rangle|\downarrow\rangle + \beta|0\rangle|\uparrow\rangle$ . After waiting for time  $\frac{\tau_L}{2}$  (half of the Larmor period), the spin state  $|0\rangle|\uparrow\rangle$  change to  $|0\rangle|\downarrow\rangle$  leaving the system in  $\alpha|1\rangle|\downarrow\rangle + \beta|0\rangle|\downarrow\rangle$ . We use the green laser with a pulse width of 130 ns to polarize the state  $|1\rangle|\downarrow\rangle$  into  $|0\rangle|\downarrow\rangle$ . From this process, we only have the initial state in the spin  $m_s = 0$  manifold. In the free precession duration on the diagram, the nuclear spin precesses with a Larmor period  $\tau_L$ , then the weak  $\pi$  pulse is used again to map the nuclear spin population back on to the electron spin state, creating the oscillation as shown in figure 4.6(b).

The graph shows the nuclear spin precession data at external magnetic field  $B_z = 46$  G with the Larmor period  $\tau_L \approx 4.49$   $\mu$ s. The peaks and dips in the signal correspond to the spin  $|\uparrow\rangle$  and spin  $|\downarrow\rangle$ , respectively. After that, we varied the magnitude of the magnetic field and observed the nuclear spin free precession show in figure

4.6(c). We fitted the graph with a linear equation  $\omega_L = \gamma_C B + \omega_0$  and obtained the gyromagnetic ratio value of the nuclear spin is equal to  $6.9 \pm 0.1$  kHz/G.

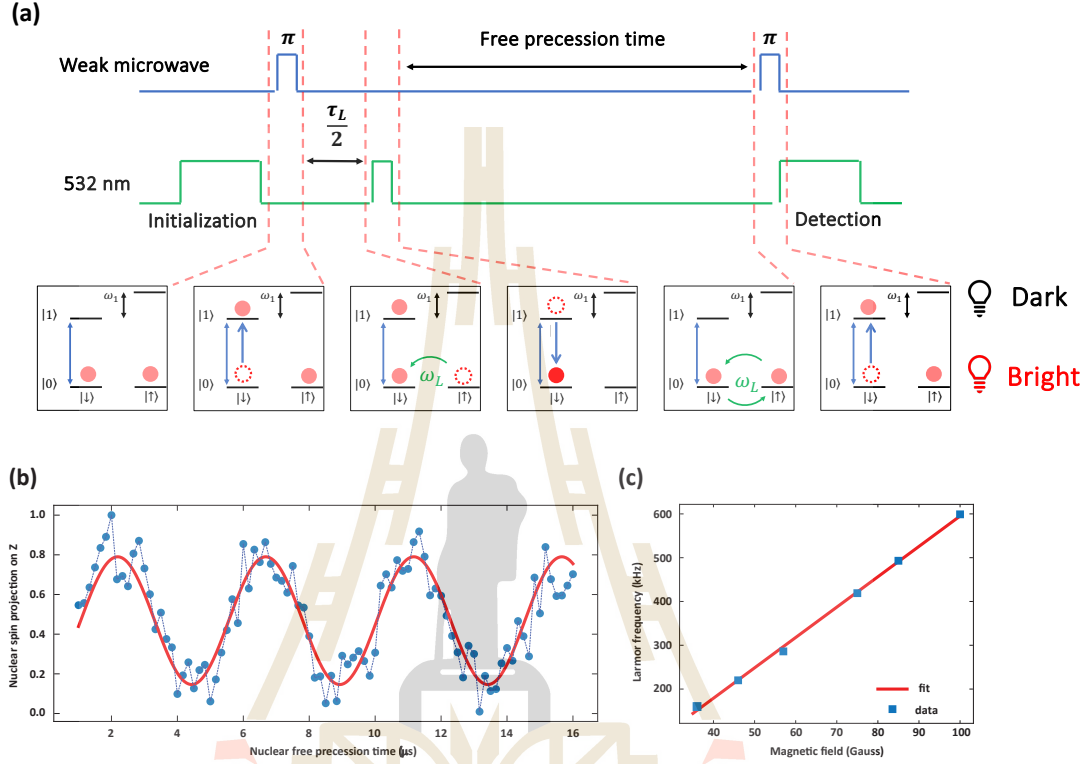


**Figure 4.6** (a) Diagram representation spin state evolution during the nuclear free precession operation, while the red circles represent the state population and green arrow show the changing of state and the blue arrow represent driving electron in weak transition. (b) Nuclear free precession graph in a magnetic field  $B_z = 46$  G. The blue dot represents experimental data, and the red line indicates the curve fitting. Nuclear spin flip from state  $|\downarrow\rangle$  to  $|\uparrow\rangle$  in every  $4.49 \mu$ s corresponding to the Larmor frequency of 220 kHz (c) The Larmor precession frequency of the single nuclear spin with a gyromagnetic ratio  $6.9 \pm 0.1$  kHz/G.

#### 4.5 Nuclear phase accumulation experiment

To access the phase rotation of the nuclear spin (the rotation of the qubit around the z axis). We use two microwave sources to observe the hyperfine effect of

the  $^{13}\text{C}$  nuclear spin. The hyperfine interaction affects nuclear spin of  $^{13}\text{C}$  let in electron spin  $|1\rangle$  manifold, making the spin  $|\uparrow\rangle$  and  $|\downarrow\rangle$  energies differ by a frequency  $\omega_1$ , which can be stored in term of phase information of the NV.

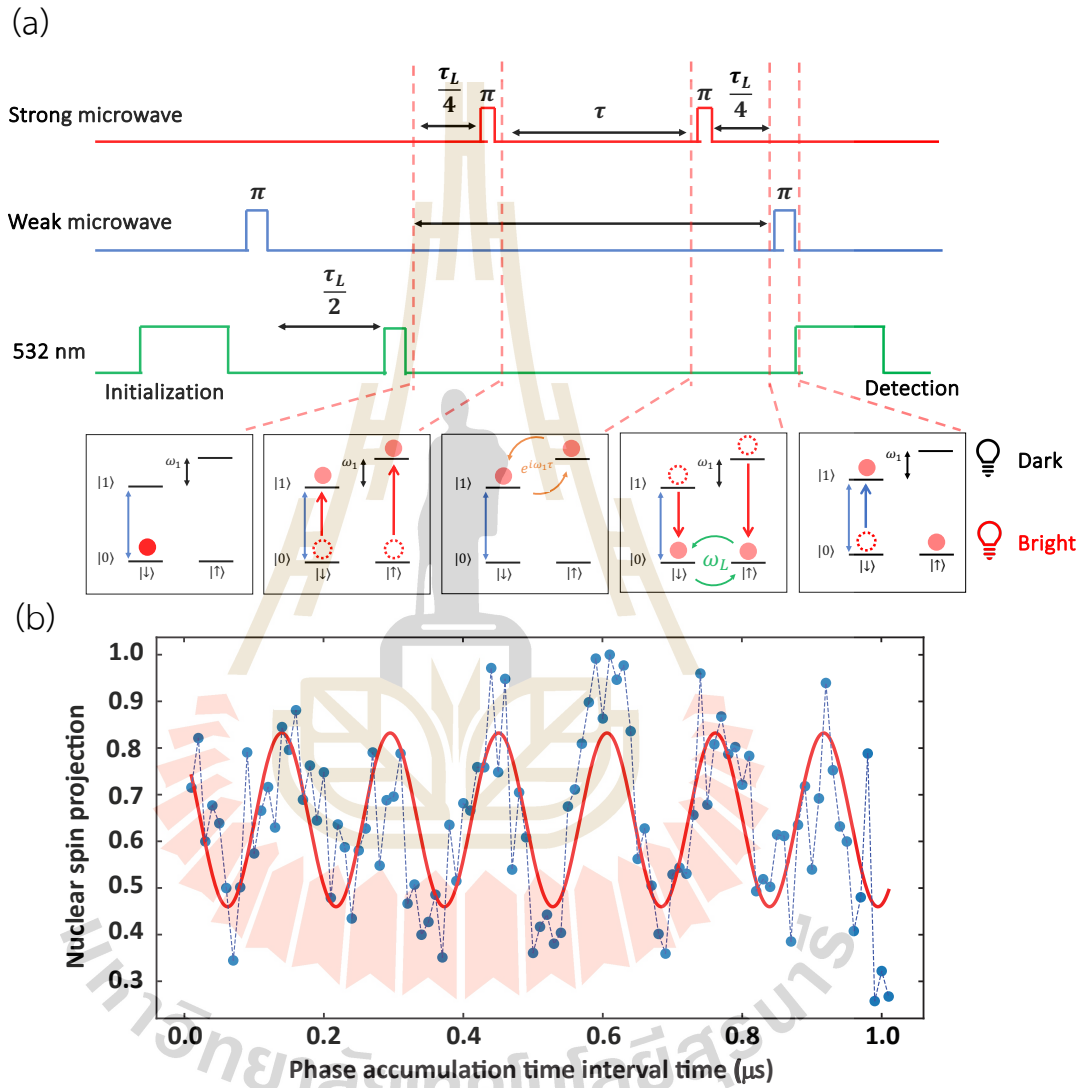


**Figure 4.7** (a) The pulse experiment diagram for observing the phase accumulation of the nuclear spin. (b) Nuclear spin projection shows oscillation with frequency  $2\pi \cdot 6.5$  MHz.

We performed the nuclear spin phase accumulation experiment followed from the pulse diagram in figure 4(a) to observe this effect. In this process, a second



microwave source is used for driving electron in both transitions with strong  $\pi$  pulse. After the state was initialized in  $|\downarrow\rangle|0\rangle$ , and then wait for the time  $\frac{\tau_L}{4}$  has elapsed, the nuclear spin precesses into the superposition state  $\frac{1}{\sqrt{2}}(|\downarrow\rangle + i|\uparrow\rangle)|0\rangle$ . Next, we applied a strong  $\pi$  pulse to drive all population of the nuclear spin into electron spin  $|1\rangle$  manifold, letting the spin state becomes  $\frac{1}{\sqrt{2}}(|\downarrow\rangle + i|\uparrow\rangle)|1\rangle$ . In the electron spin  $|1\rangle$  manifold, the nuclear spin up accumulate phase different  $\omega_1\tau$  with respect to the spin down leaving the total state in  $\frac{1}{\sqrt{2}}(|\downarrow\rangle + ie^{i\omega_1\tau}|\uparrow\rangle)|1\rangle$ . The strong  $\pi$  pulse was used again to map the state back onto the electron spin  $|0\rangle$  manifold and then, after waiting another  $\frac{\tau_L}{4}$ , we can obtain the state in form  $\frac{1}{2}((1 - e^{i\omega_1\tau})|\downarrow\rangle + i(1 + e^{i\omega_1\tau})|\uparrow\rangle)|0\rangle$ . The experimental data in figure 4.6(c) has a frequency of  $2\pi \cdot (6.5)$  MHz that corresponds to the 6.5 MHz hyperfine splitting of the  $^{13}\text{C}$  nuclear spin.

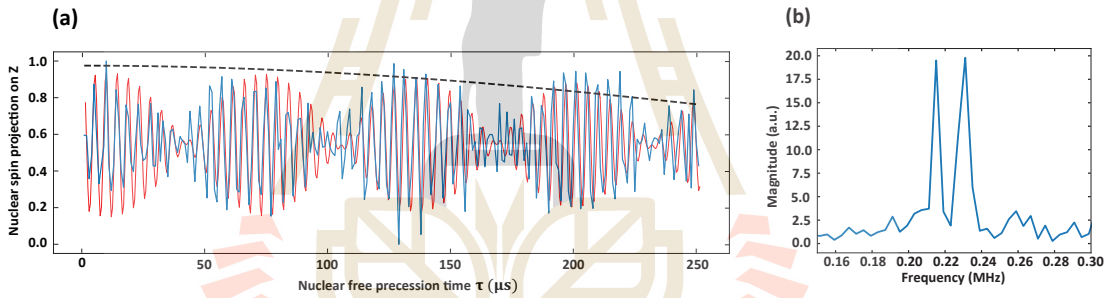


**Figure 4.8** (a) The nuclear free precession data out to 250  $\mu\text{s}$ , the blue line is the experimental data, the red line is the fitting, and the dash line shows the fitted envelope of the decay signal. (b) Nuclear spin projection shows oscillation with frequency  $2\pi \cdot (6.5)$  MHz.

#### 4.6 Nuclear spin dephasing

The free precession signals out to 250  $\mu\text{s}$  in figure 4.8(a) has a dephasing time  $T_2^* = 329 \pm 5 \mu\text{s}$ , yielding from fitting graph with a Gaussian decay model

$$P_{\uparrow} = e^{-\left(\frac{\tau}{T_2^*}\right)^4} \cdot \left( \sum_{i=1}^i A_i \cdot \cos(2\pi f_i \tau + \phi_i) \right). \quad (11)$$

Where  $P_{\uparrow}$  is the nuclear spin  $|\uparrow\rangle$  population.

$\tau$  is the free precession time of the nuclear spin.

$T_2^*$  is the nuclear spin dephasing time.

$A$  is the amplitude of the cosine function.

$f$  is the free precession frequency of the nuclear spin.

$\phi$  is the initial phase of the cosine function.

In comparison with the electron spin, this dephasing time of the nuclear spin is longer than the electron spins due to the low gyromagnetic ratio (Suter and Jelezko, 2017). However, the signal exhibits a beating behavior including in the oscillation. By performing the Fourier transform, the result in figure 4.8(b) shows two frequencies component at 0.215 MHz and 0.231 MHz, which are splitted by  $\sim 16$  kHz from each other. The beating in the free precession signal can be explained by coupling of the nuclear spin to another  $^{13}\text{C}$  nuclear spin in the diamond lattice (Dutt et al., 2007).

#### 4.7 $\pi$ phase pulse on a $^{13}\text{C}$ nuclear spin

In the free precession period of the nuclear spin, it flips from spin  $|\uparrow\rangle$  to spin  $|\downarrow\rangle$  with time  $\frac{\tau_L}{2}$ . To perform a fast  $\pi$  pulse on a  $^{13}\text{C}$  nuclear spin compared to the Larmor precession period, we use the microwave pulse sequence as shown in figure 4.9(a). After initializing the nuclear spin in state  $|\downarrow\rangle|0\rangle$ , we let the nuclear spin has a free precession with time  $\tau$ . Next, by applying the strong-pi pulse and waiting for time  $= \frac{\pi}{2\omega_1}$  (time for nuclear spin flip in spin 1 manifold). After this operation, the phase between nuclear spin  $|\downarrow\rangle$  and  $|\uparrow\rangle$  will swap, then we apply strong-pi pulse again to map the state back on the electron spin. From this schematic, we can obtain the nuclear spin  $\pi$  phase pulse during the free precession experiment. The data in figure 4.9(b) shows the comparison between the ordinary nuclear spin free precession data and the nuclear spin with  $\pi$  phase pulse after free precession  $1\ \mu\text{s}$  in the same time scale. The time used for flipping the nuclear spin state in this protocol is only around 150 ns, which is

faster than the normal Larmor precession rate that used the time around  $2.25 \mu\text{s}$  (at magnetic field  $B_z = 46 \text{ G}$ ).

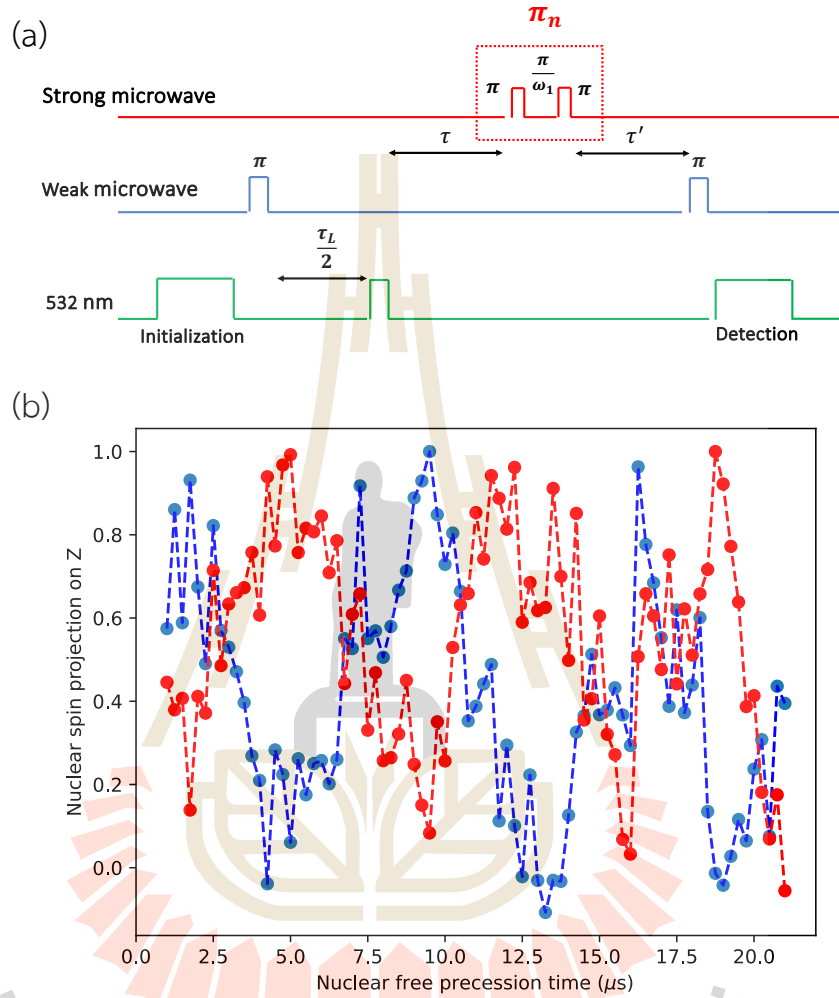


**Figure 4.9** (a) The pulse diagram for applying  $\pi$  pulse on a  $^{13}\text{C}$  nuclear spin. (b) the blue graph shows the nuclear spin free precession during time  $1 \mu\text{s} + \tau'$  without applying the nuclear spin  $\pi$  phase pulse, the red graph shows the nuclear free precession obtained by applying the  $\pi$  phase pulse on the nuclear spin after free precession  $\tau = 1 \mu\text{s}$  and then scanning time  $\tau'$ .

From the result in figure 4.8(b), the blue graph shows the nuclear spin free precession during time  $1 \mu\text{s} + \tau'$ , the red graph shows the nuclear spin echo obtained by applying the  $\pi$  pulse on the nuclear spin after free precession  $1 \mu\text{s}$  and then

scanning time  $\tau'$ . As you can see from the graph the nuclear spin state is flipped from other one. We can use this schematic to perform some operation that require the  $\pi$  pulse on the nuclear spin such as spin echo experiment.

#### 4.8 Incomplete population transfer of the nuclear spin

For the protocols that use the strong  $\pi$  pulse during the operation including section 4.4 and 4.6, the observed contrast decreases from the nuclear spin free precession population. To investigate the population loss from the system, we consider that the final state from the nuclear Ramsey experiment should be read out optically and the probability of the nuclear spin up ( $P_{\uparrow}$ ) and spin down ( $P_{\downarrow}$ ) are given by

$$P_{\uparrow} = \frac{1}{2}(1 + \cos(\omega_1\tau)) \quad (12)$$

$$P_{\downarrow} = \frac{1}{2}(1 - \cos(\omega_1\tau)) \quad (13)$$

For an ideal system, the data should have an oscillation curve shows in figure 4.9(a), which obtain from Eq. (12). The experimental data in figure 4.7(b) has a frequency of  $2\pi \cdot (6.5)$  MHz that corresponds to the 6.5 MHz hyperfine splitting. However, For the long phase accumulation duration of the  $^{13}\text{C}$  nuclear spin (out to 15  $\mu\text{s}$ ) shown in figure 4.10(b). The data shows a contrast reduction in nuclear projection data. We attribute this behavior to the imperfect transfer of the population during the use of the strong  $\pi$  pulse. The precession exhibits two beating oscillations. Fourier transformation in figure 4.10(c) shows two frequencies at 0.215 MHz and 6.5 MHz corresponding to the hyperfine splitting frequency of the  $^{13}\text{C}$  nuclear spin and the free precession frequency of the  $^{13}\text{C}$ , respectively. This proves that during the nuclear phase accumulation experiment, some nuclear spin population remained unexcited by the strong  $\pi$  pulse in the electron spin  $|0\rangle$  manifold. Childress and her team reported using this protocol but chose the spin  $m_s = +1$  manifold for state  $|1\rangle$  of the qubit. They noted that the reduced contrast probably causes from incomplete population transfer to  $m_s = +1$  because the spin population is accidental excited to  $m_s = -1$ . Conversely,

we drive the electron to  $m_s = -1$  manifold to prevent population loss, as it is difficult for the population to transition to the  $m_s = +1$  due to its higher energy. However, we still observed the population remaining in the  $m_s = 0$ . This phenomenon might be occurred due to our strong  $\pi$  pulse is still insufficient (low microwave intensity) to drive the entire population from electron spin  $m_s = 0$  to  $m_s = -1$ . Additionally, the resonance frequency for the strong  $\pi$  pulse might not perfectly match with the transition frequency because our sample contains the  $^{15}\text{N}$  spin state in the system. We can implement effective protocols to improve spin state contrast during the polarization process (Song et al., 2020).

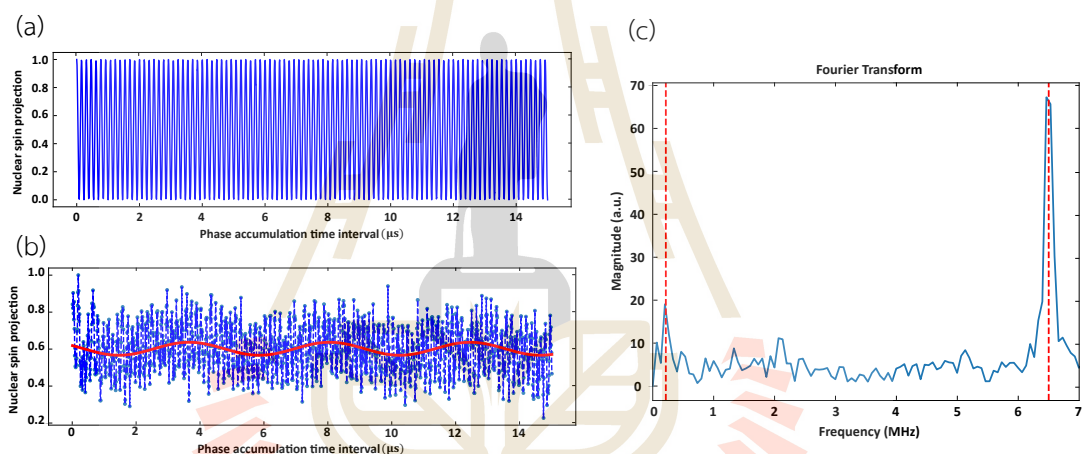


**Figure 4.10** (a) The ideal nuclear spin projection out to 15  $\mu\text{s}$  (b) The  $^{13}\text{C}$  nuclear spin phase accumulation out to 15  $\mu\text{s}$  shows two oscillations in the data. The dash line show oscillation effect from hyperfine interaction and the red line shows oscillation match with the Larmor precession frequency (c) The Fourier transform of the data in (b). The result shows the peaks at 0.215 MHz and 6.5 MHz, respectively.

## CHAPTER V

### CONCLUSION

In this thesis, we set up a home-built confocal microscope to observe the photoluminescence from the NV center, which the sub-micron resolution. Our sample was implanted with  $^{15}\text{N}$  with an energy of 30 keV and was installed into the coplanar waveguide PCB board to carrier the microwave signal for controlling the NV electron spin and  $^{13}\text{C}$  nuclear spin. The Setup can manipulate the NV system and read out the dynamics of them via optical signal. We search for the single NV center from the confocal microscope image then chose the NV near to the aluminum wire to obtain high amplitude of the microwave control field. We characterized the NV that we required for creating two qubit control by performing the experiment include pulsed-ODMR. The pulsed-ODMR showed the hyperfine effect from the  $^{13}\text{C}$  nuclear spin and  $^{15}\text{N}$  nuclear spin that can be used as a quantum register. We selected a NV center coupled with a 6.5 MHz hyperfine splitting of  $^{13}\text{C}$  nuclear to perform the indirect control of the nuclear spin. We only used a weak  $\pi$  pulse to observe the nuclear spin free precession, yielding the gyromagnetic ratio equal to  $6.9 \pm 0.1$  kHz/G and the dephasing time equal to  $514 \pm 20$   $\mu\text{s}$ . Moreover, we perform the nuclear Ramsey experiment to observe the hyperfine effect in the electronic spin  $|1\rangle$  manifold. By using the effect from the hyperfine interactions, one can perform the fast phase gate on the  $^{13}\text{C}$  nuclear compared to the bare free precession by applying the strong  $\pi$  pulse, which use the  $\pi$  pulse operation time on the nuclear spin of only 150 ns. Finally, we showed a loss of nuclear spin population during the nuclear Ramsey process due to incomplete population transfer. We demonstrated this population loss in terms of free precession in the spin  $|0\rangle$  manifold. Upon observing the long experimental process and conducting the Fourier Transform, we detected the Larmor precession included in the data, indicating effects from a non-perfectly polarized state. This will enable us to refine our experimental procedures and optimize our system to obtain the high contrast after

manipulating the nuclear spin by using the phase gate for future studies. We can improve the system by fine tuning the resonance frequency for strong and weak transitions and implementing the short green laser pulse to polarize the nuclear spin population follow from Song protocol (Song et al., 2020).





The logo of Sakon Nakhon Rajabhat University is a large, faint watermark in the center of the page. It features a golden-yellow stupa-like structure with a central figure of a person standing on a pedestal. Below the figure is an open book. The entire emblem is encircled by a ring of red, pointed shapes. The university's name in Thai is written in a grey arc at the bottom.

## REFERENCES

มหาวิทยาลัยเทคโนโลยีสุรนารี

## REFERENCES

- Bradley, C. E., Randall, J., Abobeih, M. H., Berrevoets, R. C., Degen, M. J., Bakker, M. A., ... Taminiau, T. H. (2019). A Ten-Qubit Solid-State Spin Register with Quantum Memory up to One Minute. *Physical Review X*, 9(3), 031045. doi:10.1103/PhysRevX.9.031045.
- Castelletto, S., Li, X., and Gu, M. (2012). Frontiers in diffraction unlimited optical methods for spin manipulation, magnetic field sensing and imaging using diamond nitrogen vacancy defects. *Nanophotonics*, 1(2), 139–153.
- Childress, L., Taylor, J. M., Sorensen, A. S., and Lukin, M. D. (2006). Fault-tolerant quantum communication based on solid-state photon emitters. *Physical Review Letters*, 96(7), 070504.
- Childress, L., and Hanson, R. (2013). Diamond NV centers for quantum computing and quantum networks. *MRS Bulletin*, 38.
- Childress, L., Dutt, M. V. G., Taylor, J. M., Zibrov, A. S., Jelezko, F., Wrachtrup, J., Hemmer, P. R., and Lukin, M. D. (2006). Coherent dynamics of coupled electron and nuclear spin qubits in diamond. *Science*, 314(5797), 281–285.
- Doherty, M. W., Manson, N. B., Delaney, P., Jelezko, F., Wrachtrup, J., and Hollenberg, L. C. L. (2013). The nitrogen-vacancy colour centre in diamond. *Physics Reports*, 528(1), 1–45.
- Dolde, F., Jakobi, I., Naydenov, B., Zhao, N., Pezzagna, S., Trautmann, C., ... Wrachtrup, J. (2013). Room-temperature entanglement between single defect spins in diamond. *Nature Physics*, 9(3), 139–143.
- Dréau, A., Lesik, M., Rondin, L., Spinicelli, P., Arcizet, O., Roch, J.-F., and Jacques, V. (2011). Avoiding power broadening in optically detected magnetic resonance of single NV defects for enhanced dc magnetic field sensitivity. *Physical Review B*, 84(19), 195204.

- Dutt, M. V. G., Childress, L., Jiang, L., Togan, E., Maze, J., Jelezko, F., Zibrov, A., Hemmer, P. R., and Lukin, M. D. (2007). Quantum register based on individual electronic and nuclear spin qubits in diamond. *Science*, 316(5829), 1312–1316.
- Jelezko, F., Togan, E., Maze, J., ... Lukin, M. D. (2002). Single spin states in a defect center resolved by optical spectroscopy. *Applied Physics Letters*, 81(2160).
- Grazioso, F., Patton, B., Delaney, P., Markham, M., Twitchen, D., and Smith, J. (2013). Measurement of the full stress tensor in a crystal using photoluminescence from point defects: The example of nitrogen vacancy centers in diamond. *Applied Physics Letters*, 103, 101905.
- Grover, L. K. (1997). Quantum mechanics helps in searching for a needle in a haystack. *Physical Review Letters*, 79(2), 325–328.
- Gruber, A., Drabenstedt, A., Tietz, C., Fleury, L., Wrachtrup, J., and Borczyskowski, C. v. (1997). Scanning confocal optical microscopy and magnetic resonance on single defect centers. *Science*, 276(5321), 2012–2014.
- Gupta, A., Hacquebard, L., and Childress, L. (2016). Efficient signal processing for time-resolved fluorescence detection of nitrogen-vacancy spins in diamond. *JOSAB*, 33(3), B28–B34.
- Hahn, E. L. (1950). Spin echoes. *Physical Review*, 80(4), 580–594.
- Hepler, P. K., and Gunning, B. E. (1998). Confocal fluorescence microscopy of plant cells. *Protoplasma*, 201, 121–157.
- Hong, S., Grinolds, M. S., Pham, L. M., Le Sage, D., Luan, L., Walsworth, R. L., and Yacoby, A. (2013). Nanoscale magnetometry with NV centers in diamond. *MRS Bulletin*, 38(2), 155–161.
- Ithier, G., Collin, E., Joyez, P., Meeson, P. J., Vion, D., Esteve, D., Chiarello, F., Shnirman, A., Makhlin, Y., Schrieffer, J., and Schön, G. (2005). Decoherence in a superconducting quantum bit circuit. *Physical Review B*, 72(13), 134519.
- Jamonneau, P., Lesik, M., Tetienne, J. P., Alvizu, I., Mayer, L., Dréau, A., ... Jacques, V. (2016). Competition between electric field and magnetic field noise in the decoherence of a single spin in diamond. *Physical Review B*, 93(2), 024305.

- Jeske, J., Lau, D. W. M., Vidal, X., McGuinness, L. P., Reineck, P., Johnson, B. C., ... Greentree, A. D. (2017). Stimulated emission from nitrogen-vacancy centres in diamond. *Nature Communications*, 8(1), 14000.
- Doherty, J. C. McCallum, S. Onoda, F. Jelezko, T. Ohshima, T. Volz, J. H. Cole, B. C. Gibson, and Greentree, A. D. (2017). Stimulated emission from nitrogen-vacancy centres in diamond. *Nature Communications*, 8(1), 14000.
- Jiang, L., Hodges, J. S., Maze, J. R., Maurer, P., Taylor, J. M., Cory, D. G., Hemmer, P. R., Walsworth, R. L., Yacoby, A., Zibrov, A. S., and Lukin, M. D. (2009). Repetitive readout of a single electronic spin via quantum logic with nuclear spin ancillae. *Science*, 326(5950), 267–272.
- Kagami, S., Shikano, Y., and Asahi, K. (2011). Detection and manipulation of single spin of nitrogen-vacancy center in diamond toward application of weak measurement. *Physica E: Low-Dimensional Systems and Nanostructures*, 43(3), 761–765.
- Maurer, P. C., Kucsko, G., Latta, C., Jiang, L., Yao, N. Y., Bennett, S. D., ... Lukin, M. D. (2012). Room-temperature quantum bit memory exceeding one second. *Science*, 336(6086).
- Nakahara, M., and Ohmi, T. (2008). *Quantum computing: From linear algebra to physical realizations* (1st ed.). CRC Press.
- Manson, N. B., Harrison, J. P., and Sellars, M. J. (2006). The nitrogen-vacancy center in diamond re-visited. eprint/0601360.
- Nie, S., Chiu, D. T., and Zare, R. N. (1994). Probing individual molecules with confocal fluorescence microscopy. *Science*, 266(5187), 1018–1021.
- Nielsen, M. A., and Chuang, I. L. (2004). *Quantum computation and quantum information*. Cambridge University Press. ISBN 978-0-521-63503-5.
- Robledo, L., Bernien, H., van der Sar, T., and Hanson, R. (2011). Spin dynamics in the optical cycle of single nitrogen-vacancy centres in diamond. *New Journal of Physics*, 13(2), 025013.
- Sangtawesin, S., Brundage, T. O., and Petta, J. R. (2014). Fast room-temperature phase gate on a single nuclear spin in diamond. *Physical Review Letters*, 113(2), 020506.

- Sangtawesin, S., Dwyer, B. L., Srinivasan, S., Allred, J. J., Rodgers, L. V. H., De Greve, K., ... de Leon, N. P. (2019). Origins of diamond surface noise probed by correlating single-spin measurements with surface spectroscopy. *Physical Review X*, 9(3), 031052.
- Sewani, V., Vallabhapurapu, H., Yang, Y., Firgau, H., Adambukulam, C., Johnson, B., Pla, J., and Laucht, A. (2020). Coherent control of NV- centers in diamond in a quantum teaching lab. *American Journal of Physics*, 88, 1156–1169.
- Smeltzer, B., Childress, L., and Gali, A. (2011).  $^{13}\text{C}$  hyperfine interactions in the nitrogen-vacancy centre in diamond. *New Journal of Physics*, 13(2), 025021.
- Song, Y., Tian, Y., Hu, Z., Zhou, F., Xing, T., Lu, D., ... Du, J. (2020). Pulse-width-induced polarization enhancement of optically pumped NV electron spin in diamond. *Photonics Research*, 8(8), 1289–1295.
- Storteboom, J., Dolan, P., Castelletto, S., Li, X., and Gu, M. (2015). Lifetime investigation of single nitrogen vacancy centres in nanodiamonds. *Optics Express*, 23(9), 11327–11333.
- Suter, D., and Jelezko, F. (2017). Single-spin magnetic resonance in the nitrogen-vacancy center of diamond. *Progress in Nuclear Magnetic Resonance Spectroscopy*, 98, 50–62.
- Taminiau, T. H., Wagenaar, J. J. T., van der Sar, T., Jelezko, F., Dobrovitski, V. V., and Hanson, R. (2012). Detection and control of individual nuclear spins using a weakly coupled electron spin. *Physical Review Letters*, 109(13), 137602.
- Toyli, D., Casas, C., Christle, D., Dobrovitski, V., and Awschalom, D. (2013). Fluorescence thermometry enhanced by the quantum coherence of single spins in diamond. *Proceedings of the National Academy of Sciences of the United States of America*, 110.
- Waldherr, G., Wang, Y., Zaiser, S., Jamali, M., Schulte-Herbrueggen, T., Abe, H., Ohshima, T., Isoya, J., Du, J., and Neumann, P. (2014). Quantum error correction in a solid-state hybrid spin register. *Nature*, 506.
- Zhang, J., Hegde, S. S., and Suter, D. (2019). Improved indirect control of nuclear spins in diamond N-V centers. *Physical Review Applied*, 12(6), 064047.

Zhang, S., and Li, L. (2022). A brief introduction to quantum algorithms. *CCF Transactions on High Performance Computing*, 4(1), 53–62.



## CURRICULUM VITAE

**Name:** Kritsana Saego

**Date of Birth:** 30 April 1998

**Place of Birth:** Rayong, Thailand

**Educations:**

- 2017-2021: Department of Physics, Science, Mahidol University, Nakhon Pathom, Thailand (Bachelor of Science)
- 2022-2024: School of Physics, Science, Suranaree University of technology, Nakhon Ratchasima, Thailand (Master of Science)

**Grants and Fellowship:**

Development and Promotion of Science and Technology Talents Project (DPST)

**Publications:**

**Saego, K** and Sangtawesin, S. (2025). Indirect control of  $^{13}\text{C}$  nuclear spin in nitrogen vacancy center in diamond. Journal of Physics: Conference Series, 2934, 012021.

Rasritat, A., Tapakidareekul, M., **Saego, K.**, Meevasana, W., and Sangtawesin, S. (2024). Formation of oxygen protective layer on monolayer MoS<sub>2</sub> via low energy electron irradiation. RSC Advances, 14, 21999.